



# COLDz: Deep 34 GHz Continuum Observations and Free–Free Emission in High-redshift Star-forming Galaxies

H. S. B. Algera<sup>1</sup> , J. A. Hodge<sup>1</sup> , D. Riechers<sup>2,3</sup> , E. J. Murphy<sup>4</sup> , R. Pavesi<sup>2</sup> , M. Aravena<sup>5</sup> , E. Daddi<sup>6</sup> , R. Decarli<sup>7</sup> ,  
M. Dickinson<sup>8</sup> , M. Sargent<sup>9</sup> , C. E. Sharon<sup>10</sup> , and J. Wagg<sup>11</sup>

<sup>1</sup> Leiden Observatory, Leiden University, P.O. Box 9513, 2300 RA Leiden, The Netherlands; [algera@strw.leidenuniv.nl](mailto:algera@strw.leidenuniv.nl)

<sup>2</sup> Department of Astronomy, Cornell University, Ithaca, NY 14853, USA

<sup>3</sup> Max-Planck Institute for Astronomy, Königstuhl 17, D-69117 Heidelberg, Germany

<sup>4</sup> National Radio Astronomy Observatory, 520 Edgemont Road, Charlottesville, VA 22903, USA

<sup>5</sup> Núcleo de Astronomía, Facultad de Ingeniería y Ciencias, Universidad Diego Portales, Av. Ejército 441, Santiago, Chile

<sup>6</sup> Laboratoire AIM, CEA/DSM-CNRS-Université Paris Diderot, Irfu/Service d'Astrophysique, CEA Saclay, Orme des Merisiers, F-91191, Gif-sur-Yvette cedex, France

<sup>7</sup> INAF—Osservatorio di Astrofisica e Scienza dello Spazio di Bologna, via Gobetti 93/3, I-40129 Bologna, Italy

<sup>8</sup> NSF's National Optical-Infrared Astronomy Research Laboratory (NOIRLab), 950 North Cherry Avenue, Tucson, AZ 85719, USA

<sup>9</sup> Astronomy Centre, Department of Physics and Astronomy, University of Sussex, Brighton BN1 9QH, UK

<sup>10</sup> Yale-NUS College, 16 College Avenue West 01-220, 138527 Singapore

<sup>11</sup> SKA Organization, Lower Withington Macclesfield, Cheshire SK11 9DL, UK

Received 2020 December 15; revised 2021 February 9; accepted 2021 February 14; published 2021 May 6

## Abstract

The high-frequency radio sky has historically remained largely unexplored due to the typical faintness of sources in this regime, and the modest survey speed compared to observations at lower frequencies. However, high-frequency radio surveys offer an invaluable tracer of high-redshift star formation, as they directly target the faint radio free–free emission. We present deep continuum observations at 34 GHz in the COSMOS and GOODS-North fields from the Karl G. Jansky Very Large Array (VLA), as part of the COLDz survey. The deep COSMOS mosaic spans  $\sim 10$  arcmin<sup>2</sup> down to  $\sigma = 1.3 \mu\text{Jy beam}^{-1}$ , while the wider GOODS-N observations cover  $\sim 50$  arcmin<sup>2</sup> to  $\sigma = 5.3 \mu\text{Jy beam}^{-1}$ . We detect a total of 18 galaxies at 34 GHz, of which nine show radio emission consistent with being powered by star formation; although for two sources, this is likely due to thermal emission from dust. Utilizing deep ancillary radio data at 1.4, 3, 5, and 10 GHz, we decompose the spectra of the remaining seven star-forming galaxies into their synchrotron and thermal free–free components, and find typical thermal fractions and synchrotron spectral indices comparable to those observed in local star-forming galaxies. We further determine free–free star formation rates (SFRs), and show that these are in agreement with SFRs from spectral energy distribution-fitting and the far-infrared/radio correlation. Our observations place strong constraints on the high-frequency radio emission in typical galaxies at high redshift, and provide some of the first insights into what is set to become a key area of study with future radio facilities, such as the Square Kilometer Array Phase 1 and next-generation VLA.

*Unified Astronomy Thesaurus concepts:* High-redshift galaxies (734); Galaxy evolution (594); Galaxy formation (595); Radio continuum emission (1340)

## 1. Introduction

Deep radio observations offer an invaluable view on star formation in the high-redshift universe. With current facilities, such as the upgraded National Science Foundation's (NSF's) Karl G. Jansky Very Large Array (VLA), both star-forming galaxies and faint active galactic nuclei (AGNs) can now be studied down to microjansky flux densities at gigahertz frequencies. However, a regime that remains substantially understudied is the faint radio population at high frequencies ( $\nu \gtrsim 10$  GHz), which is in large part the result of the comparative inefficiency at which high-frequency radio surveys can be executed. First, for a fixed telescope size, the field of view of a single pointing decreases steeply with frequency as  $\nu^{-2}$ . Second, radio sources are generally intrinsically fainter at high radio frequencies,  $S_\nu \propto \nu^\alpha$ , where  $\alpha \sim -0.7$  (Condon 1992), and third, typically only a modest fraction of telescope observing time is suitable for high-frequency observations due to more stringent requirements on the observing conditions. As a result, the survey speed at 34 GHz is  $\gtrsim 5000$  times smaller compared to observations at the more commonly utilized frequency of 1.4 GHz.

Despite these observational difficulties, high-frequency radio observations provide complementary insight into both star-forming galaxies and AGNs. Historically, low-frequency radio observations have been used as a tracer of star formation activity through the far-infrared/radio correlation (FIRRC; van der Kruit 1971, 1973; de Jong et al. 1985; Helou et al. 1985). This correlation, which has been shown to hold over several orders of magnitude in terms of luminosity (Yun et al. 2001; Bell 2003), as well as to high redshift ( $z \sim 5$ ; Calistro Rivera et al. 2017; Delhaize et al. 2017; Algera et al. 2020a; Delvecchio et al. 2021), relates the predominantly nonthermal synchrotron emission of a star-forming galaxy to its far-infrared (FIR) luminosity. The latter has been well-calibrated as a tracer of star formation, as at FIR-wavelengths, dust re-emits the light absorbed from young, massive stars (e.g., Kennicutt 1998). The synchrotron emission, instead, emanates from cosmic rays accelerated by supernova-induced shocks, and as such constitutes a tracer of the end product of massive-star formation (Condon 1992; Bressan et al. 2002). However, a second process is expected to dominate the radio spectral energy distribution (SED) at high frequencies ( $\nu \gtrsim 30$  GHz): radio

free-free emission (FFE). Unlike radio synchrotron radiation, FFE is a much more direct star formation rate (SFR) tracer, as it originates from the H II regions in which massive stars have recently formed. In addition, unlike other commonly used probes of star formation such as UV continuum emission or the hydrogen Balmer lines, FFE constitutes a tracer of star formation that is largely unbiased by dust extinction. These characteristics establish FFE as one of the most reliable tracers of star formation, both in the local and the high-redshift universe.

Locally, the radio spectra of both individual star-forming regions and star-forming galaxies have been well characterized, and have established FFE as a means of calibrating other tracers of star formation (Murphy et al. 2011). In addition, in nearby galaxies, FFE can typically be separated spatially from nonthermal synchrotron emission, as individual extragalactic star-forming regions can be resolved (Tabatabaei et al. 2013; Querejeta et al. 2019; Linden et al. 2020). However, in the high-redshift universe, FFE has remained elusive, despite the observational advantage that high-frequency continuum emission redshifts into radio bands that are more easily accessible from Earth, facilitating the sampling of the free-free-dominated regime of the radio spectrum. The comparative faintness of high-redshift galaxies, however, complicates the usage of FFE as a tracer of star formation at early cosmic epochs. Indeed, current detections of high-frequency continuum emission in distant galaxies remain limited to bright or gravitationally lensed starbursts (Thomson et al. 2012; Aravena et al. 2013; Riechers et al. 2013; Wagg et al. 2014; Huynh et al. 2017; Penney et al. 2020). In addition, most of these studies lacked the ancillary low-frequency data required to robustly disentangle FFE from the overall radio continuum, which requires observations at a minimum of three frequencies (e.g., Tabatabaei et al. 2017; Klein et al. 2018), or probed rest-frame frequencies dominated by thermal emission from dust ( $\nu \gtrsim 200$  GHz; Condon 1992). Despite this observational complexity, one of the key science goals for upcoming radio facilities such as the next-generation VLA is to systematically use FFE as a probe of star formation in the high-redshift galaxy population (Barger et al. 2018). As such, it is already of considerable interest to explore this high-frequency parameter space with current radio facilities.

While radio continuum observations are invaluable in characterizing high-redshift star formation in a dust-unbiased manner, radio surveys are additionally capable of detecting what fuels this process, namely molecular gas. For a clear census of the molecular gas reservoir of the universe, blind surveys are crucial, as they do not suffer from any biases arising from follow-up radio observations of known high-redshift sources. The first such blind surveys have recently been completed, such as the ALMA Spectroscopic Survey in the Hubble Ultra-Deep Field (ASPECS; Walter et al. 2016; Decarli et al. 2016), and the CO Luminosity Density at High Redshift survey (COLDz; Pavesi et al. 2018; Riechers et al. 2019, 2020), which targets low- $J$  CO observations at 34 GHz using the VLA. Due to the large bandwidth of its high-frequency receivers, deep VLA surveys of molecular gas result in sensitive continuum images essentially “for free.” In this work, we describe the deep continuum observations of the COLDz survey. Our main goal is to constrain the radio spectra of typical sources in a frequency range that has not been widely explored, and extend our analysis to a new parameter space of

faint AGNs and star-forming galaxies, down to the microjansky level. The COLDz survey covers a region of two well-studied extragalactic fields, COSMOS (Scoville et al. 2007) and GOODS-North (Giavalisco et al. 2004), and hence allows for a multiwavelength perspective on this faint population.

The outline of this paper is as follows. In Section 2 we describe our 34 GHz VLA observations and the creation of deep continuum images, as well as the existing ancillary multiwavelength data. We outline the detection and source extraction of sources at 34 GHz in Section 3, and assign the radio sample multiwavelength counterparts and redshifts in Section 4. We present our deep radio number counts at 34 GHz in Section 5, and separate the sample into radio AGNs and star-forming galaxies in Section 6. In Section 6, we additionally decompose the spectra of the star-forming galaxies into radio synchrotron and FFE, and compare the latter as a tracer of star formation with more commonly adopted tracers at high redshift. Section 7 provides an outlook for the future, and discusses how upcoming radio facilities will revolutionize high-redshift studies of radio star formation. Finally, we summarize our findings in Section 8. Where necessary, we assume a standard  $\Lambda$ -cold dark matter cosmology, with  $H_0 = 70 \text{ km s}^{-1} \text{ Mpc}^{-1}$ ,  $\Omega_m = 0.30$ , and  $\Omega_\Lambda = 0.70$ . Magnitudes are quoted in the AB-system, and a Chabrier (2003) initial mass function is assumed.

## 2. Observations and Data Reduction

### 2.1. COLDz

The COLDz survey (Pavesi et al. 2018; Riechers et al. 2019, 2020) was designed to blindly probe the low- $J$  CO-lines in high-redshift galaxies, which requires high-frequency observations spanning a large bandwidth. Both are provided by the Ka band of the upgraded VLA, which allows for a total of 8 GHz of contiguous frequency coverage, tuneable to be within the range of 26.5–40.0 GHz. The COLDz observing strategy is presented in Pavesi et al. (2018), to which we refer the reader for additional details.

For the optimal constraints on the CO luminosity function, COLDz combines a deep yet small mosaic in the COSMOS field with wider but shallower observations in the GOODS-N field. The COSMOS observations constitute a seven-pointing mosaic, and account for a total on-source time of 93 hr. The data were taken in the VLA D (82 hr) and DnC (11 hr) configurations, and span a total frequency range of 30.969–39.033 GHz, using dual polarization. The observations of the GOODS-N field comprise a total of 122 hr of on-source time, and make up a 57-pointing mosaic. The data were predominantly taken in the D-configuration (83.5 hr), with additional observations taking place in the D  $\rightarrow$  DnC (4.4 hr), DnC (30.8 hr), and DnC  $\rightarrow$  C (3 hr) configurations. The observations cover a frequency range between 29.981–38.001 GHz, and in what follows, we will refer to both the COSMOS and GOODS-N observations by their typical central frequency of 34 GHz.

Calibration of the observations was done in CASA version 4.1.0, with extensive use being made of a modified version of the VLA pipeline, the details of which can be found in Pavesi et al. (2018). As one of the main goals of COLDz is to detect spectral lines, both Hanning smoothing and RFLAG, used to remove radio frequency interference (RFI), were switched off. Instead, some persistent RFI at 31.5 GHz was flagged manually, and some occasions of narrow noise spikes were flagged via the methods

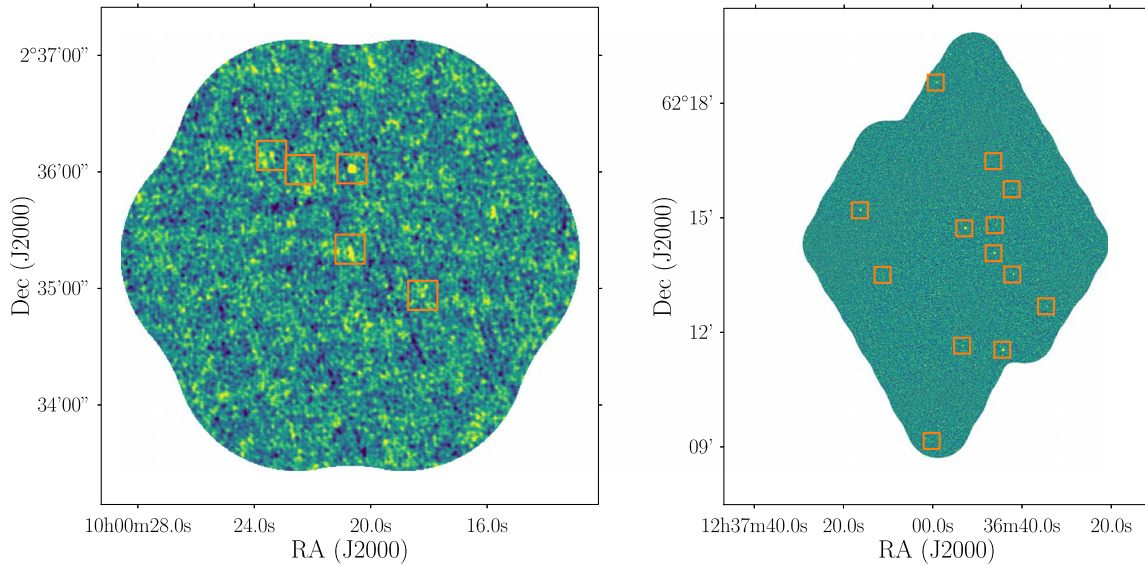


**Figure 1.** Left: the seven-pointing COSMOS 34 GHz continuum mosaic of  $\sim 10$  arcmin<sup>2</sup>. The five robust detections (Section 3) are highlighted via orange squares. Right: the  $\sim 50$  arcmin<sup>2</sup> GOODS-North 34 GHz mosaic (pointings 1–56), with the 13 robust detections highlighted. Both mosaics are uncorrected for primary beam attenuation, and the color scale runs from  $-\sigma$  to  $3\sigma$ , where  $\sigma$  represents the (uncorrected) rms noise in the image. It is clear that many 34 GHz detections lie close to the  $3\sigma$  detection threshold, and would not have been identified without deep, ancillary radio data across the fields.

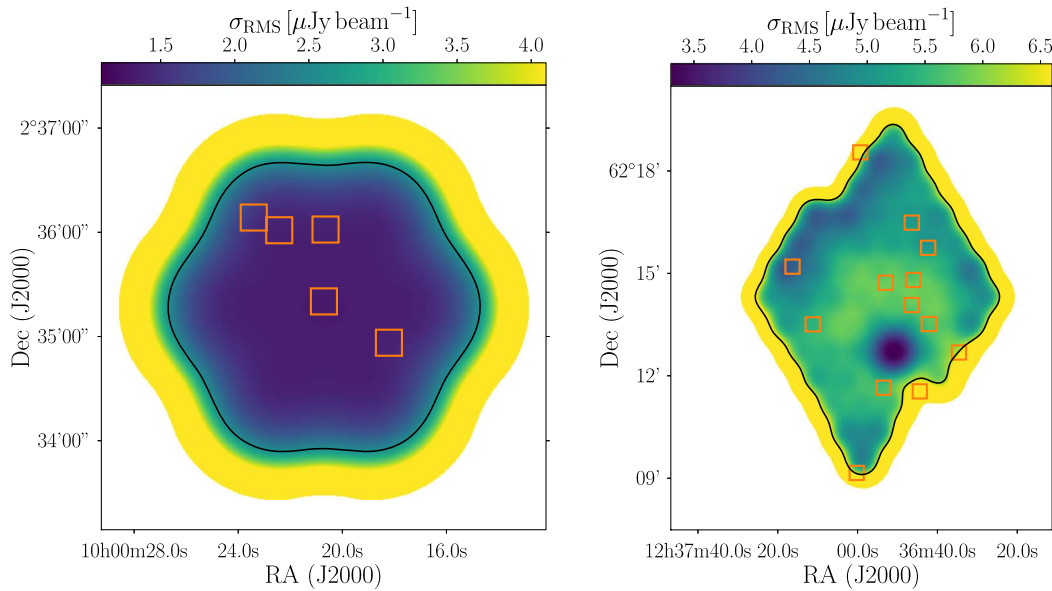


**Figure 2.** Left: the COLDz COSMOS rms map, after correction for primary beam attenuation. The uncorrected rms map is highly uniform, and any structure in the map is solely the result of the beam correction. Right: the rms map of the 34 GHz observations across the GOODS-N field. The map uncorrected for the beam is highly uniform in its noise properties, and the structure in the map indicates the differences in observing time across the mosaic, with a single deep pointing centered on R.A. = 12:36:51.06, decl. = +62:12:43.8, designed to overlap with the Plateau de Bure Interferometer observations from Decarli et al. (2014), highlighted as the region with the lowest rms. The black lines outlining the mosaics indicate the region where the primary beam reaches 50% of its maximum sensitivity, and the robust detections in both fields are highlighted via the orange boxes, as in Figure 1.

detailed in Pavesi et al. (2018). The data were then concatenated, and, for the continuum observations presented here, subsequently averaged in time (9 s) and frequency (16 channels), in order to reduce the size of the data set prior to imaging. The imaging of the calibrated 34 GHz observations was carried out in CASA version 4.3.1, using the “mosaic” mode of CASA task CLEAN. For both the COSMOS and the GOODS-N mosaics, a multifrequency synthesis algorithm was employed to take into account the large bandwidth of the observations. A natural weighting was further adopted, in order to maximize the sensitivity of the data. The data were imaged iteratively, by cleaning all sources at  $> 6\sigma$  down to the  $2\sigma$  level.

We present the 34 GHz continuum maps across the COSMOS and GOODS-N fields, as well as the corresponding rms noise maps, in Figures 1 and 2. The COSMOS mosaic covers a field of view of 9.6 arcmin<sup>2</sup> out to 20% of the peak primary beam sensitivity. The central rms noise in the image equals  $1.3 \mu\text{Jy beam}^{-1}$ , with the typical rms increasing to  $1.5$  and  $1.9 \mu\text{Jy beam}^{-1}$ , within 50% and 20% of the peak primary beam sensitivity, respectively. The synthesized beam of the COSMOS observations is well described by an elliptical Gaussian of  $2''.70 \times 2''.41$  with a position angle of  $-0^\circ.7$ .

The GOODS-N mosaic spans an area of 51 arcmin<sup>2</sup> out to 20% of the peak primary beam sensitivity, covering roughly

one-third of the “traditional” GOODS-N survey (Giavalisco et al. 2004). The typical noise level varies slightly across the mosaic, with a single, deep 34 GHz pointing in the field reaching a central noise level of  $3.2 \mu\text{Jy beam}^{-1}$ . Across the entire GOODS-N field, within 50% and 20% of the peak primary beam sensitivity, respectively, the typical rms noise equals  $5.3 \mu\text{Jy beam}^{-1}$  and  $5.5 \mu\text{Jy beam}^{-1}$ . The synthesized beam is well described by an elliptical Gaussian of  $2''.19 \times 1''.84$ , with a position angle of  $75^\circ.3$ , after smoothing the different pointings to a common beam. Pavesi et al. (2018) also provide a version of the GOODS-N radio map where all pointings have been imaged at their native resolution. While the resulting mosaic cannot be described by a single beam, it allows for the search for unresolved sources at slightly higher signal-to-noise ratios (S/Ns), as no smoothing or tapering was required. We use this “unsmoothed” map for source detection in Section 3, in addition to the regular mosaic with a homogenized beam.

## 2.2. Ancillary Radio Observations

The COLDz observations in the COSMOS field overlap in their entirety with deep 3 and 10 GHz VLA pointings from the COSMOS-XS survey (Algera et al. 2020b; van der Vlugt et al. 2021). These images have a resolution similar to COLDz, with a synthesized beam of  $2''.14 \times 1''.81$   $2''.14 \times 1''.81$  and  $2''.33 \times 2''.01$  at 3 and 10 GHz, respectively. At 3 GHz, the observations reach a central rms of  $0.53 \mu\text{Jy beam}^{-1}$ , with a typical primary beam sensitivity of 90% of the maximum across the COLDz mosaic. The 10 GHz data reach a central rms sensitivity of  $0.41 \mu\text{Jy beam}^{-1}$  (typical primary beam sensitivity of 80%), and were centered on the COLDz observations by design. In total, 70 sources detected at 3 GHz at  $\geq 5\sigma$  fall within the  $\sim 10 \text{ arcmin}^2$  COLDz field of view. A subset of 40 are additionally detected at 10 GHz. In addition, the central region of the COSMOS field, spanning  $\approx 1 \text{ deg}^2$ , is covered by VLA observations at 1.4 GHz (Schinnerer et al. 2007, 2010). These observations reach a typical rms sensitivity of  $12 \mu\text{Jy beam}^{-1}$  across the COLDz field of view, at a resolution of  $1''.5 \times 1''.4$ . In total, two sources within the COLDz field of view are detected at 1.4 GHz. Adopting a typical spectral index of  $\alpha = -0.70$ , the COLDz and 1.4 GHz COSMOS observations are approximately of equal relative depth.<sup>12</sup>

The GOODS-N field is similarly well covered by radio observations from the VLA. At 1.4 GHz, the entire field has been imaged in a single pointing by Owen (2018), down to a central rms of  $2.2 \mu\text{Jy beam}^{-1}$  with little variation across the field of view of the COLDz mosaic. The resolution of the radio data equals  $1''.6$ , and a total of 186 sources detected at 1.4 GHz by Owen (2018) fall within the 20% power point of the GOODS-N COLDz image. The field has additionally been mapped at 5 GHz by Gim et al. (2019). They detect 52 sources down to an rms of  $3.5 \mu\text{Jy beam}^{-1}$  across two VLA pointings covering a total area of  $109 \text{ arcmin}^2$ , which fully overlaps with the COLDz footprint. Their angular resolution of  $1''.47 \times 1''.42$  is similar to that of the deeper 1.4 GHz observations, and Gim et al. (2019) find that all 5 GHz detections have a counterpart in this lower-frequency map. Finally, Murphy et al. (2017)

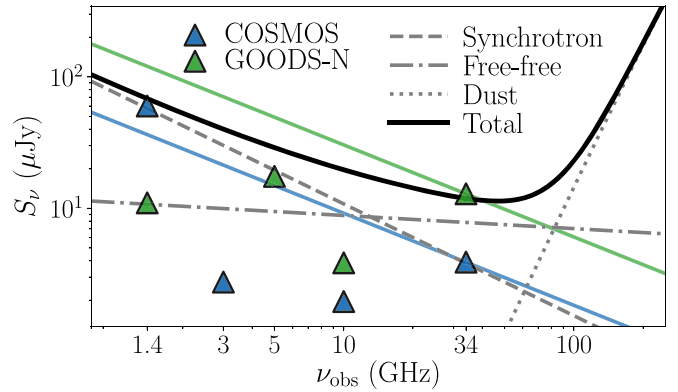


**Figure 3.** The detection limits of the various radio observations across COSMOS and GOODS-N, superimposed on the radio spectrum of a star-forming galaxy ( $\text{SFR} = 100 M_\odot \text{ yr}^{-1}$  at  $z = 1$ ; see the text for details). The blue (green) lines indicate the detection limit of the COLDz 34 GHz continuum data, scaled with a typical  $\alpha = -0.70$ . The different constituents of the radio spectrum are shown, including free-free emission, which is expected to become dominant at rest-frame  $\nu \gtrsim 30 \text{ GHz}$ . As such, the COLDz observations directly target the strongly free-free-dominated regime.

present a single pointing at 10 GHz in the GOODS-N field (primary beam FWHM of  $4''.25$ ) at a native resolution of  $0''.22$ . At this high angular resolution, their observations reach a sensitivity of  $0.57 \mu\text{Jy beam}^{-1}$  in the center of the pointing. Murphy et al. (2017) further provide two tapered images with a resolution of  $1''$  and  $2''$ , similar to the ancillary radio data in the field. These images reach an rms noise of  $1.1$  and  $1.5 \mu\text{Jy beam}^{-1}$ , respectively. In total, Murphy et al. (2017) recover 38 sources across the combined high-resolution and tapered images. Approximately 75% of the COLDz GOODS-N data overlap with the smaller pointing at 10 GHz, when imaged out to 5% of the primary beam FWHM (Murphy et al. 2017).

We summarize the detection limits of the various radio observations across both COSMOS and GOODS-N in Figure 3, and compare these with the typical radio spectrum of a star-forming galaxy ( $\text{SFR} = 100 M_\odot \text{ yr}^{-1}$  at  $z = 1$ ). This assumes the Kennicutt (1998) conversion between SFR and infrared luminosity, adapted for a Chabrier IMF, as well as a simple optically thin dust SED with  $\beta = 1.8$  and  $T_{\text{dust}} = 35 \text{ K}$ . We further adopt the Condon (1992) model for the radio spectrum of star-forming galaxies, and assume the FIRRC from Delhaize et al. (2017). Under these assumptions, a galaxy with  $\text{SFR} = 100 M_\odot \text{ yr}^{-1}$  can be directly detected at 34 GHz out to  $z = 2$  ( $z = 1$ ) in the COSMOS (GOODS-N) field.

## 2.3. Ultraviolet to Submillimeter Observations

Both the COSMOS and GOODS-North fields have been targeted by a wealth of multiwavelength observations, spanning the full X-ray to radio regime. For the COSMOS field, we adopt the multiwavelength matching procedure for the COSMOS-XS survey (Algera et al. 2020b), as all 34 GHz continuum detections have radio counterparts in this survey (Section 3). This cross-matching procedure invokes the recent “Super-deblended” catalog from Jin et al. (2018), who adopt a novel deblending technique to address confused mid-infrared to submillimeter observations. The Super-deblended catalog provides photometry from Spitzer/IRAC  $3.6 \mu\text{m}$  to MAMBO  $1.2 \text{ mm}$  (for a full list of references, see Jin et al. 2018), as well as radio data at 1.4 and 3 GHz from Schinnerer et al. (2010) and Smolčić et al. (2017), respectively. However, we directly

<sup>12</sup> However, we note that we adopt a  $3\sigma$  detection threshold for the COLDz data in Section 3, whereas a  $5\sigma$  threshold was adopted by Schinnerer et al. (2007) for the 1.4 GHz observations. As such, sources detected at  $3\sigma$  in the COLDz survey require a spectral index of  $\alpha \lesssim -0.85$  to additionally be detected at 1.4 GHz.

adopt the radio fluxes from the 1.4 GHz catalog from Schinnerer et al. (2007, 2010), and use the deeper COSMOS-XS 3 GHz data in favor of the observations from Smolčić et al. (2017). In addition, Algera et al. (2020b) cross-match with the  $z^{++}YJHK_s$ -selected COSMOS2015 catalog from Laigle et al. (2016) containing far-ultraviolet to near-infrared photometry, in order to complete the coverage of the SED. Finally, we search for Atacama Large Millimeter/submillimeter Array (ALMA) counterparts as part of the AS2COSMOS (Simpson et al. 2020) and A3COSMOS surveys (Liu et al. 2019), which constitute a collection of individual pointings across the COSMOS field.

A wealth of multiwavelength data similarly exist across the GOODS-N field. In order to obtain optical/near-infrared photometry for the 34 GHz continuum detections, we adopt the 3D-HST photometric catalog from Skelton et al. (2014). Source detection was performed in a deep combined F125W+F140W+F160W image, and further photometry is carried out in the wavelength range of 0.3–8  $\mu\text{m}$ , including Spitzer/IRAC observations from Dickinson et al. (2003) and Ashby et al. (2013). For further details, we refer the reader to Skelton et al. (2014). We obtain additional mid- and far-infrared photometry from the Super-deblended catalog across the GOODS-N field by Liu et al. (2018). They adopt combined priors from Spitzer/IRAC, Spitzer/MIPS 24  $\mu\text{m}$  and VLA 1.4 GHz observations, and utilize these to deblend the photometry at more strongly confused wavelengths. The Super-deblended catalog provides additional photometry from the Spitzer/Infrared Spectrograph (IRS), Herschel/Photodetector Array Camera and Spectrometer (PACS; Magnelli et al. 2013) and Herschel/Spectral and Photometric Imaging REceiver (SPIRE; Elbaz et al. 2011), as well as data from JCMT/SCUBA-2 850  $\mu\text{m}$  (Geach et al. 2017) and AzTEC+MAMBO 1.2 mm (Penner et al. 2011).

#### 2.4. X-Ray Observations

While a radio-based selection renders one sensitive to AGN activity at radio wavelengths,  $\sim 20\%$ – $25\%$  of the faint radio population ( $S_{1.4} \lesssim 1 \text{ mJy}$ ; equivalent to  $S_{34} \lesssim 100 \mu\text{Jy}$  given  $\alpha = -0.70$ ) is thought to consist of radio-quiet AGNs (Bonzini et al. 2013; Smolčić et al. 2017). These sources show no substantial AGN-related emission at radio wavelengths, but are instead classified as AGNs based on signatures at other wavelengths. Strong X-ray emission, in particular, forms an unmistakable manifestation of AGN activity. As such, we make use of the deep X-ray coverage over both the COSMOS and GOODS-N fields to characterize the nature of the 34 GHz continuum detections.

The COSMOS field is covered in its entirety by the 4.6 Ms Chandra COSMOS Legacy survey (Civano et al. 2016), with the individual Chandra pointings accounting for a typical  $\approx 160$  ks of exposure time. The area covered by the COLDz survey contains three X-ray detections, at a typical detection limit of the survey of  $\sim 2 \times 10^{-15} \text{ erg cm}^{-2} \text{ s}^{-1}$  in the full range of 2–10 keV. The catalog provided by Marchesi et al. (2016) further includes X-ray luminosities for X-ray detections with robust optical and infrared counterparts.

The GOODS-North field is similarly covered by deep 2 Ms Chandra observations as part of the Chandra Deep Field North Survey (Xue et al. 2016). Across the COLDz field of view, the survey identifies 189 X-ray sources, and attains a flux limit of  $\sim 3.5 \times 10^{-17} \text{ erg cm}^{-2} \text{ s}^{-1}$  in the 0.5–7 keV energy range—nearly a factor of 50 deeper than the COSMOS data, when converted to the same energy range adopting  $\Gamma = 1.8$ . The

catalog provided by Xue et al. (2016) further includes X-ray luminosities for the entries with reliable redshift information.

### 3. Continuum Sources

We run source detection on our 34 GHz radio maps using PYBDSF (Mohan & Rafferty 2015), prior to correcting the images for the primary beam. This has the benefit that the noise properties are uniform across the mosaics, which facilitates source detection, and additionally ensures that fewer spurious sources arise around the noisy edges of the maps.<sup>13</sup> In our source detection procedure, we can afford to set a liberal detection threshold, as both the COSMOS and GOODS-N fields contain additional low-frequency radio data of greater depth relative to the COLDz observations, and as such we expect any 34 GHz detections to have radio counterparts. In this work, we therefore adopt a  $3\sigma$  peak detection threshold for both images.

In the COSMOS field, we compare to the deep S- and X-band observations from van der Vlugt et al. (2021). For a source to be undetected in this 10 GHz map, yet detected at 34 GHz, requires a highly inverted spectral index of  $\alpha_{34}^{10} \gtrsim 0.55$ . In the GOODS-N field, we compare with the 1.4 GHz observations from Owen (2018), and find that 34 GHz sources require an inverted spectral index of  $\alpha_{34}^{1.4} \gtrsim 0.15$  to remain undetected in the lower-frequency map. We note that, as we perform source detection at low S/Ns, the source sizes calculated via PYBDSF may be affected by the local noise properties within the images. In particular, sources with fitted radio sizes smaller than the synthesized beam will have an integrated flux density smaller than the peak value, and will have an uncertainty on the latter that is smaller than the local rms noise in the map (Condon 1997). We show in Appendix A.2 that all but one source are likely to be unresolved at  $\sim 2''$  resolution. For all unresolved sources, we adopt the peak brightness, while the integrated flux density is used otherwise. Following the discussion above, we redefine the uncertainty on the peak brightness and conservatively adopt the maximum of the calculated uncertainty from PYBDSF and the local rms at the source position.

In the COSMOS map, we detect 57 peaks at  $\geq 3\sigma$  within 20% of the peak primary beam sensitivity (Figure 4). We can match six to COSMOS-XS counterparts within  $0''.7$ , where we expect to have  $N_{\text{false}} = 0.2$  false matches based on randomly shifting the coordinates of all  $\geq 3\sigma$  peaks in the mosaic, and repeating the matching a large number of times. This radius was chosen to include all close associations to COSMOS-XS sources, while minimizing the number of expected false matches ( $N_{\text{false}} \ll 1$ ). To further verify the robustness of the six close counterparts, we run our source detection procedure on the inverted radio map (i.e., multiplied by  $-1$ ), and find a total of 60 negative “sources,” all of which are by definition spurious. None of these can be matched to COSMOS-XS counterparts within  $0''.7$ , indicating the real matches are likely to be robust. However, out of the six associations to COSMOS-XS galaxies within  $0''.7$ , we find that one candidate source (S/N = 3.3 at 34 GHz) is detected solely at 3 GHz while a 10 GHz counterpart is also expected, implying it is likely to be spurious. As such, we discard it from our sample and retain five sources that form the robust COSMOS continuum sample.

<sup>13</sup> We have verified that, after applying the primary beam correction, the flux densities are consistent with those obtained from running source detection on the primary-beam-corrected map, with a typical ratio of  $S_{\text{uncorr}}/S_{\text{corr}} = 1.05 \pm 0.07$ .

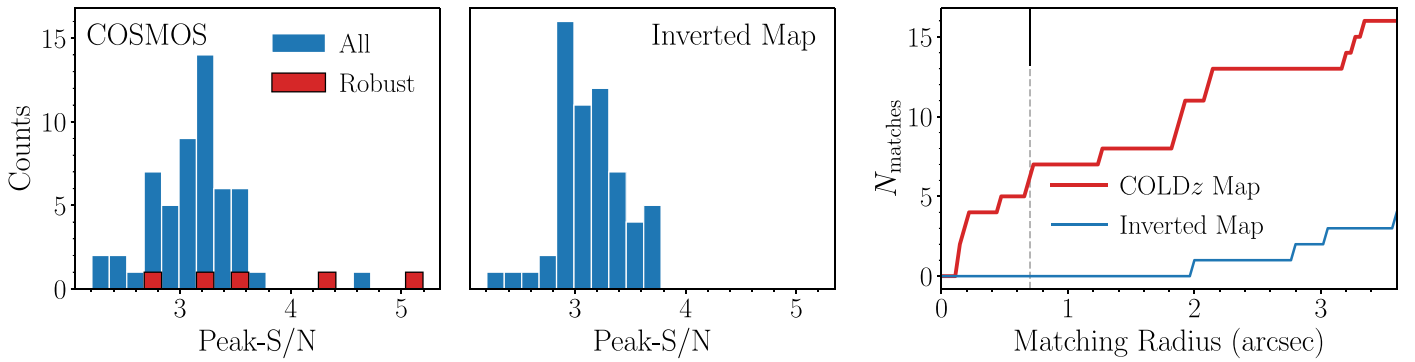


**Figure 4.** Left: distribution of S/Ns for all of the peaks identified in the COSMOS 34 GHz image. Sources with lower-frequency radio counterparts within  $0''.7$  are highlighted in red. The most significant detection at a 34 GHz  $S/N = 17$  is not shown for clarity. Middle: same as the left panel, now showing “sources” detected in the inverted image. No matches within  $0''.7$  are found with lower-frequency radio counterparts, and no spurious detection above  $S/N = 3.7$  exists. Right: number of cross-matches between the 34 GHz continuum detections and the detections in the deeper 3 GHz COSMOS-XS map, as a function of matching radius. The radius adopted in this work is indicated via the black vertical line. No spurious matches are found in the inverted map out to  $\sim 2''$ , indicating that the sources recovered in the 34 GHz map are likely to be real.

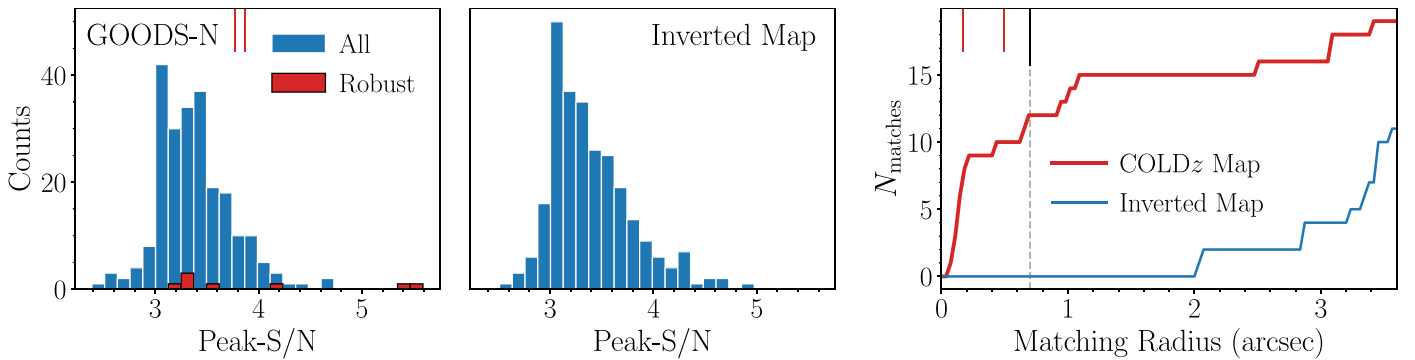


**Figure 5.** Same as Figure 4, now showing peaks identified in the GOODS-N radio map. Four high-S/N detections in the real map are not shown for clarity, and the two red, vertical dashes indicate the two additional sources we recover when performing source detection in the unsmoothed radio map (see the text for details). In total, 13 sources are robustly detected at 34 GHz in GOODS-N.

Three of these have an S/N larger than the highest peak S/N in the inverted radio map of  $3.7\sigma$ . The remaining two have a relatively low S/N of  $\sim 3.5$ , but are deemed robust due to their multiwavelength associations.

We adopt an identical source detection procedure for the GOODS-N 34 GHz map. In total, PYBDSF identifies 236 peaks above  $3\sigma$  in the map, of which we match 12 with low-frequency radio counterparts in the catalog from Owen (2018) at  $0''.7$ , where we expect  $N_{\text{false}} = 0.3$  incorrect identifications. We find 263 sources in the inverted radio map, none of which are matched to lower-frequency radio counterparts within  $0''.7$ . However, upon cross-matching our 12 robust sources with the 5 GHz catalog from Gim et al. (2019), we find only 11 matches within  $0''.7$ . The single unmatched source ( $S/N = 3.3$  at 34 GHz) also falls within the field of view of the single deep X-band pointing from Murphy et al. (2017), but is additionally undetected at 10 GHz. As such, this source is likely to be spurious, and we discard it from further analysis. The S/N distributions of all peaks identified by PYBDSF in the GOODS-N image and its inverted counterpart are shown in Figure 5. The maximum S/N in the inverted map is  $S/N \approx 5.0$ , which implies that 5/11 robust 34 GHz detections lie below the most significant spurious source. This emphasizes the added value of the deep, low-frequency data, which allow us to identify faint sources that would not have been recovered in a blind source detection procedure. We further perform source detection via PYBDSF on the unsmoothed mosaic (Section 2), using the same detection threshold as adopted for the regular GOODS-N

mosaic, in order to maximize the number of recovered sources. We find two additional matches with low-frequency counterparts at both 1.4 and 5 GHz, resulting in a total of 13 sources identified in GOODS-N. We adopt the peak brightness for these two sources, given the lack of a common beam in the unsmoothed mosaic, and use the local rms in the map as the appropriate uncertainty.

Given that we require any identifications at 34 GHz to have robust low-frequency radio counterparts, we may be missing sources with highly unusual inverted spectra. To investigate this possibility, we median-stack in the low-frequency radio maps on the positions of the highest signal-to-noise peaks at 34 GHz for which no radio counterpart was found (3 and 10 GHz in COSMOS, 1.4 GHz in GOODS-N, using the publicly available radio map from Morrison et al. 2010). In neither the COSMOS nor the GOODS-N fields do we see any evidence for a positive signal in the stacks, indicating that most—and likely all—of these  $S/N \approx 3$ –5 peaks at 34 GHz are spurious. In addition, we cross-match the peaks in the 34 GHz map that do not have radio counterparts with optical/near-infrared-selected sources from the COSMOS2015 and 3D-HST catalogs in COSMOS and GOODS-N, respectively, within  $0''.7$ . We find two matches with the COSMOS2015 catalog, at  $\sim 0''.4$ . However, based on a visual inspection, there is no hint of emission at either 3 or 10 GHz for these sources, indicating that they are likely to be spurious. We find 37 matches within  $0''.7$  between  $\geq 3\sigma$  peaks in the 34 GHz GOODS-N radio map without radio counterparts and the 3D-HST catalog. In addition to a visual inspection, we stack these sources at

**Table 1**  
Radio Properties of the 34 GHz Selected COLDz Sample

ID	R.A. (deg)	Decl. (deg)	$z^a$	$S_{1.4}^b$ ( $\mu$ Jy)	$S_3$ ( $\mu$ Jy)	$S_5$ ( $\mu$ Jy)	$S_{10}$ ( $\mu$ Jy)	$S_{34}^c$ ( $\mu$ Jy)
COLDz-cont-COS-1	150.093436	2.600324	0.89	$< 60.0$	$8.8 \pm 0.6$	...	$5.4 \pm 0.5$	$3.2 \pm 1.4$
COLDz-cont-COS-2 <sup>d</sup>	150.086281	2.588947	5.30	$< 60.0$	$21.9 \pm 0.6$	...	$9.1 \pm 0.4$	$6.8 \pm 1.3$
COLDz-cont-COS-3	150.086022	2.600442	$0.98 \pm 0.01$	$272.0 \pm 13.0$	$159.1 \pm 0.6$	...	$78.2 \pm 0.5$	$23.6 \pm 1.4$
COLDz-cont-COS-4 <sup>e</sup>	150.075874	2.582339	2.48	$< 60.0$	$17.8 \pm 0.6$	...	$7.6 \pm 0.5$	$4.3 \pm 1.4$
COLDz-cont-COS-5	150.097512	2.602361	1.00	$< 60.0$	$27.4 \pm 0.6$	...	$11.3 \pm 0.5$	$6.3 \pm 1.5$
COLDz-cont-GN-1	189.318274	62.253407	0.56	$175.4 \pm 5.9$	...	$153.0 \pm 3.7$	$133.0 \pm 12.9$	$72.3 \pm 4.3$
COLDz-cont-GN-2 <sup>f</sup>	189.251020	62.152715	$1.61^{+0.27}_{-0.01}$	$297.4 \pm 10.1$	...	$114.2 \pm 5.3$	...	$25.4 \pm 6.4$
COLDz-cont-GN-3	189.247233	62.309206	$2.00^{+0.02}_{-0.01}$	$4600.8 \pm 78.0$	...	$1106.0 \pm 6.0$	...	$42.7 \pm 7.6$
COLDz-cont-GN-4	189.222491	62.194332	1.27	$74.4 \pm 7.6$	...	$19.7 \pm 3.5$	$17.4 \pm 2.1$	$15.3 \pm 5.7$
COLDz-cont-GN-5	189.220371	62.245561	0.32	$214.0 \pm 7.8$	...	$188.1 \pm 3.5$	$191.5 \pm 3.5$	$185.7 \pm 11.4$
COLDz-cont-GN-6	189.193081	62.234673	0.96	$278.2 \pm 9.4$	...	$177.7 \pm 3.5$	$138.9 \pm 2.9$	$79.4 \pm 5.8$
COLDz-cont-GN-7 <sup>g</sup>	189.191979	62.246903	$2.95^{+0.06}_{-0.02}$	$103.9 \pm 3.7$	...	$42.6 \pm 8.3$	$35.1 \pm 2.9$	$15.4 \pm 5.8$
COLDz-cont-GN-8	189.184957	62.192532	1.01	$1792.0 \pm 76.2$	...	$963.0 \pm 6.3$	$449.8 \pm 5.8$	$317.8 \pm 8.2$
COLDz-cont-GN-9	189.176004	62.262621	0.86	$185.0 \pm 7.2$	...	$46.3 \pm 4.3$	$39.0 \pm 2.8$	$15.6 \pm 5.1$
COLDz-cont-GN-10	189.175494	62.225399	2.02	$461.3 \pm 6.9$	...	$137.8 \pm 3.5$	$67.0 \pm 2.2$	$30.6 \pm 5.7$
COLDz-cont-GN-11 <sup>h</sup>	189.143948	62.211490	1.22	$188.5 \pm 7.7$	...	$59.8 \pm 3.4$	$31.5 \pm 2.4$	$17.6 \pm 6.5$
COLDz-cont-GN-12	189.297011	62.225238	2.00	$126.0 \pm 6.3$	...	$46.6 \pm 8.1$	$16.3 \pm 2.6$	$18.1 \pm 5.4$
COLDz-cont-GN-13	189.193158	62.274894	0.50	$403.0 \pm 14.2$	...	$95.9 \pm 12.4$	$26.0 \pm 4.8$	$18.0 \pm 5.1$

#### Notes.

<sup>a</sup> Uncertainties are quoted on the photometric redshifts only.

<sup>b</sup> Where applicable,  $5\sigma$  upper limits are quoted for the COSMOS field, based on the typical rms in the 1.4 GHz map (Schinnerer et al. 2007, 2010).

<sup>c</sup> Flux densities are corrected for flux boosting (Appendix A.3). The flux densities listed for COLDz-cont-COS-2 and COLDz-cont-COS-4 are predominantly due to the combination of a bright CO-line and dust continuum emission (Section 6.3).

<sup>d</sup> Detected in CO(2–1) emission in the COLDz survey as COLDz.COS.0 (Pavesi et al. 2018); also known as AzTEC-3.

<sup>e</sup> Detected in CO(1–0) emission in the COLDz survey as COLDz.COS.2 (Pavesi et al. 2018).

<sup>f</sup> Identified as GN-16 in the submillimeter observations by Pope et al. (2005).

<sup>g</sup> Identified as GN-12 by Pope et al. (2005).

<sup>h</sup> Identified as GN-26 by Pope et al. (2005); has a CO(2–1)-based redshift from Frayer et al. (2008).

1.4 GHz, but find no detection in the stack, and place a  $3\sigma$  upper limit on the average 1.4 GHz emission of  $S_{1.4} \leq 2.7 \mu\text{Jy beam}^{-1}$ , which corresponds to a highly inverted  $\alpha_{34}^{1.4} \gtrsim 0.6$ . This further substantiates that the majority of the low-S/N peaks identified at 34 GHz are likely to be spurious.

We summarize the radio properties of the 18 sources detected at 34 GHz in Table 1, and show postage stamps on top of HST images in Figure 6. The tabulated flux densities are further corrected for flux boosting, as outlined in Appendix A.3. For a source detected at  $3\sigma$  ( $4\sigma$ ), the typical correction factor is 20% (10%), whereas at  $S/N \gtrsim 5$ , the effects of flux boosting are found to be negligible.

## 4. Multiwavelength Properties

### 4.1. Multiwavelength Counterparts and Redshifts

Across the combined COSMOS and GOODS-N 34 GHz mosaics, we identify a total of 18 robust high-frequency continuum detections. In this section, we detail the association of multiwavelength counterparts to this radio-selected sample. For the five COSMOS sources, we follow the cross-matching procedure from Algera et al. (2020b). We first match the 34 GHz continuum detections to the Super-deblended catalog containing FIR photometry, exploring matching radii up to  $0''.9$ . However, we find that all five sources can be matched to Super-deblended counterparts within  $0''.3$ , where we expect a negligible number of false associations. We further find that the five sources can be additionally cross-matched to galaxies in the COSMOS2015 catalog, similarly within  $0''.3$ . We subsequently cross-match with the AS2COSMOS and A3COSMOS

ALMA catalogs, finding a single match at  $0''.1$  that appears in both catalogs, and adopt the photometry from the former. We additionally match with the robust and tentative catalog of COLDz CO-emitters from Pavesi et al. (2018) and recover two matches within  $0''.3$  within the robust set of blind CO-detections.<sup>14</sup>

We then extract the optimal photometric or spectroscopic redshift from these catalogs. We prioritize redshifts in the following order: (1) a spectroscopic value based on a COLDz CO-line, (2) a spectroscopic redshift within the Super-deblended catalog, and (3) a photometric redshift within the COSMOS2015 catalog. In total, we find that four out of five COLDz COSMOS detections have a spectroscopically confirmed redshift, while the remaining source has a well-constrained photometric redshift measurement (COLDz-cont-COS-3 at  $z = 0.98 \pm 0.01$ ). We note that one of our 34 GHz continuum detections (COLDz-cont-COS-2) is the well-studied submillimeter galaxy AzTEC.3 at  $z = 5.3$ , which is additionally detected in CO-emission in the COLDz survey. For AzTEC.3, we further compile additional available ALMA continuum photometry at 230 and 300 GHz from Pavesi et al. (2016).

For the GOODS-N field, we follow a similar procedure. We first cross-match the COLDz continuum detections with the 3D-HST survey (Brammer et al. 2012; Skelton et al. 2014; Momcheva et al. 2016), adopting the radio positions at 1.4 GHz from Owen (2018), as these are of higher signal-to-noise than the 34 GHz data, and as such are less susceptible to the local

<sup>14</sup> As such, the observed 34 GHz continuum emission may be in part due to these bright CO-lines. We investigate this in Section 6.3.

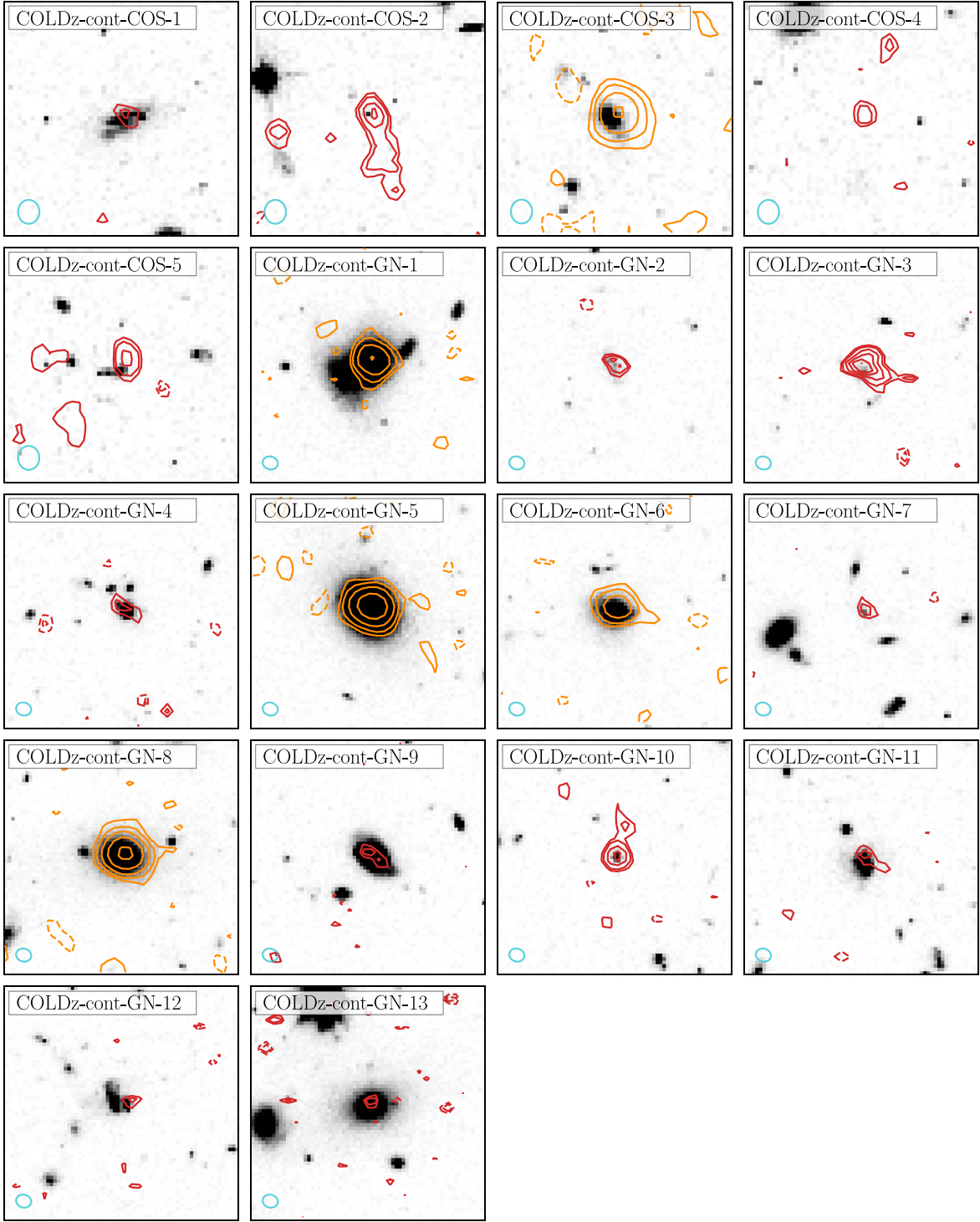


**Figure 6.** Postage stamps ( $16'' \times 16''$ ) of the 18 robust COLDz detections, overlaid on HST F814W (COSMOS) or F160W (GOODS-N) images. For faint sources ( $S/N \leq 10$  at 34 GHz), 34 GHz contours are shown in red, and represent  $\pm 2.5\sigma$ , followed by  $\pm 3\sigma, \pm 4\sigma, \dots$  in steps of  $1\sigma$ , where  $\sigma$  represents the local rms in the radio map. Bright sources—typically radio AGNs, as will be quantified in Section 6.1—are shown via orange contours, in steps of  $\pm 2^N\sigma$ , where  $N = 1, 2, \dots$ . Negative contours are shown via dashed lines, and the beam size is indicated in the lower left corner via the cyan ellipse. While half of the sample is detected at relatively low S/Ns ( $3\text{--}5\sigma$ ), most of these are star-forming galaxies, likely dominated at these frequencies by radio free-free emission (Section 6.2), and form the focus of this work.

noise properties. We find that all 13 radio sources have counterparts in the 3D-HST survey within  $0''.3$ , where no spurious matches are expected. We subsequently cross-match with the Super-deblended catalog, and find that all but one of the 34 GHz continuum sources have a counterpart at FIR wavelengths. All 12 cross-matches have a Super-deblended counterpart within  $0''.3$ , while there are no further matches

within  $3''.0$  of the single unmatched entry. We further find three cross-matches within  $0''.1$  with the catalog of submillimeter-selected galaxies from Pope et al. (2005), which we identify with GN12, GN16, and GN26, the latter of which has a spectroscopically measured redshift of  $z = 1.22$  based on a CO(2–1) detection from Frayer et al. (2008). Additional matching with the COLDz catalog of line emitters in the

GOODS-N field does not result in further matches. As such, the  $z=5.3$  submillimeter galaxy GN10 (Daddi et al. 2009; Riechers et al. 2020), detected in COLDz as the brightest CO-emitter (Pavesi et al. 2018), remains undetected in deep 34 GHz imaging. Upon performing photometry at the known position of GN10, we determine a peak brightness of  $S_{34} = 11.0 \pm 5.6 \mu\text{Jy beam}^{-1}$  ( $\approx 2\sigma$ ), placing it well below our survey detection limit.

We compile the optimal redshifts for the 13 GOODS-N 34 GHz continuum sources in a similar manner as for the COSMOS field. In order of priority, we adopt a spectroscopic redshift from the Super-deblended catalog, or the best redshift from 3D-HST (Momcheva et al. 2016), the latter being either a spectroscopic redshift from HST grism, or a photometric redshift from Skelton et al. (2014). We further overwrite a single spectroscopic value for COLDz-cont-GN-10 at  $z = 4.424$  with the updated value of  $z = 2.018$ , based on the discussion in Murphy et al. (2017). Overall, 10/13 sources have a spectroscopically confirmed redshift, while the remaining three sources have a well-constrained photometric redshift.

#### 4.2. Spectral Energy Distributions

We use SED-fitting code MAGPHYS (da Cunha et al. 2008, 2015) to determine the physical properties of the 34 GHz continuum detections. MAGPHYS adopts an energy balance technique to couple the stellar emission at ultraviolet to near-infrared wavelengths to thermal dust emission at longer wavelengths, and as such, it models the ultraviolet to FIR SED in a self-consistent way. This is additionally useful for sources lacking FIR photometry; as in this case, shorter wavelengths will still provide constraints on the total dust emission. While MAGPHYS is also capable of modeling the radio spectrum of star-forming galaxies, we do not utilize any observations at wavelengths beyond 1.3 mm in our SED-fitting procedure, as any emission from an AGN at radio wavelengths is not incorporated in the fitting. We additionally add a 10% uncertainty in quadrature to the cataloged flux density uncertainties blueward of Spitzer/MIPS 24  $\mu\text{m}$ , following, e.g., Battisti et al. (2019). This accounts for uncertainties in the photometric zero-points, and further serves to guide the fitting into better constraining the FIR part of the SED. Via MAGPHYS, we obtain several physical properties for our galaxies, including FIR luminosities, SFRs, and stellar masses. We show the fitted SEDs for all 18 COLDz continuum detections in Figure 17 in Appendix B, and tabulate their physical parameters in Table 4.

#### 4.3. X-Ray and Mid-infrared AGN Signatures

Given that the COLDz continuum detections in the COSMOS field are all identified in the COSMOS-XS survey, we adopt the results from Algera et al. (2020b), who match the COSMOS-XS 3 GHz continuum sources with the X-ray catalog from Marchesi et al. (2016). None of the five COLDz COSMOS continuum sources, however, have counterparts in X-ray emission within a separation of  $1''.4$ , and as such, we calculate upper limits on their X-ray luminosity adopting  $\Gamma = 1.8$ . However, as the resulting limits are of modest depth, we cannot state definitively whether the COLDz COSMOS sources are X-ray AGNs. We note, however, that all of them fall below the typical X-ray emission seen in submillimeter galaxies (Alexander et al. 2005), which in turn are thought to

predominantly be star formation dominated. We additionally adopt the criteria from Donley et al. (2012) in order to identify AGNs at  $z \leq 2.7$  through the mid-infrared signature ascribed to a dusty torus surrounding the accreting black hole, and similarly find no signature of AGN-related emission at mid-infrared wavelengths. We limit ourselves to this redshift range, as at higher redshifts, the Donley et al. (2012) criteria are susceptible to false positives in the form of dusty star-forming galaxies (e.g., Stach et al. 2019).

For the GOODS-N field, we find 11/13 matches with the X-ray catalog from Xue et al. (2016), within a separation of  $1''.0$ . At this matching radius, no false identifications are expected. We compare the X-ray luminosities with the emission expected from star formation, adopting the relations from Symeonidis et al. (2014). This comparison classifies nine sources as AGNs based on their X-ray emission, despite two of these sources having  $[0.5-8]$  keV X-ray luminosities below the typical threshold for AGNs of  $L_X = 10^{42} \text{ erg s}^{-1}$ . We additionally find that only a single X-ray detected source exhibits mid-infrared colors that place it within the Donley et al. (2012) wedge. Overall, we conclude that the majority of 34 GHz continuum detections in the GOODS-N field are X-ray AGNs. Due to the COSMOS X-ray data being comparatively shallower, we cannot assess definitively whether the five 34 GHz continuum sources in the COSMOS field are similarly AGNs based on their X-ray emission. However, a lower AGN fraction in COSMOS is expected, as its radio observations are significantly deeper than in GOODS-N, and the incidence rate of AGNs is a strong function of radio flux density (Smolčić et al. 2017; Algera et al. 2020b). Regardless, if X-ray AGNs are present in the COLDz/COSMOS detections, they are unlikely to be dominating the SED.

### 5. 34 GHz Source Counts

Radio number counts, while historically used as a probe for the cosmology of the universe, remain a useful tool for comparing surveys, in addition to visualizing the onset of different radio populations. At the bright end ( $S_{1.4} \gg 1 \text{ mJy}$ ), the Euclidean number counts decline smoothly toward lower flux densities, and are dominated by luminous radio AGNs (e.g., Condon & Mitchell 1984). At 1.4 GHz, the number counts show a flattening at  $S_{1.4} \approx 1 \text{ mJy}$ , believed to be the advent of star-forming galaxies and radio-quiet AGNs as the dominant radio populations (e.g., Rowan-Robinson et al. 1993; Seymour et al. 2004; Padovani et al. 2009; Smolčić et al. 2017). For a typical spectral index of  $\alpha = -0.70$ , this flattening should arise around  $S_{34} \approx 100 \mu\text{Jy}$ , and hence is covered in the range of flux densities probed in this work. We note that these flux densities may be “contaminated” by thermal emission from dust, or in the case of two COSMOS sources, by bright CO-emission, which are typically not an issue in low-frequency radio source counts. However, while we correct for this when examining the radio spectra of the star-forming COLDz continuum detections in detail (Section 6.2), here we compute the number counts based on the raw observed flux densities.

As we adopt deep radio observations as prior positions for possible 34 GHz continuum sources, we expect our sample to be fully reliable, i.e., not to contain any spurious detections. However, our sample may still be incomplete, in particular as a result of the rms of our radio maps increasing rapidly toward the image edges due to the enhanced primary beam attenuation (Figure 2). In turn, in these regions we may miss faint 34 GHz

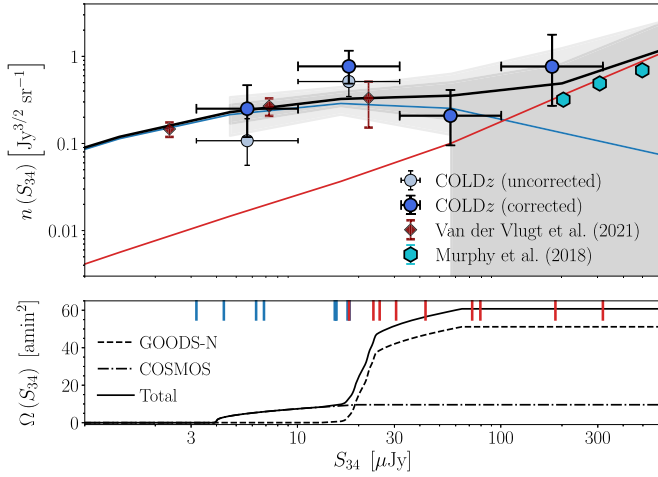


**Figure 7.** Upper: completeness-corrected Euclidean-normalized radio source counts at 34 GHz across the combined COSMOS and GOODS-N mosaics. The purple diamonds show the 10 GHz counts from van der Vlugt et al. (2021), and the cyan hexagons represent the 28.5 GHz counts from Murphy & Chary (2018), both rescaled to 34 GHz assuming  $\alpha = -0.70$ . The blue and red lines indicate the scaled source counts for star-forming galaxies and AGNs from the Bonaldi et al. (2019) simulations at 20 GHz, respectively. The dark (light) gray regions indicate the expected  $1\sigma$  ( $2\sigma$ ) level of cosmic variance, which drops to zero at low flux densities when our effective area is zero. Lower: the effective area of the COLDz observations as a function of flux density. For  $S_{34} \lesssim 20 \mu\text{Jy}$ , we are restricted to the relatively small field of view of the COLDz COSMOS observations. The blue (red) vertical bars indicate the (deboosted) 34 GHz flux density at which a star-forming galaxy (radio AGN) is detected (Section 6). Despite the relatively large uncertainties, our 34 GHz number counts are in good agreement with (rescaled) measurements and predictions in the literature.

continuum sources that would have been observed had the rms been constant across our field of view. As such, we adopt the fractional incompleteness as a function of radio flux density as determined from inserting mock sources into our radio maps (Appendix A.1). Denoting the completeness at flux density  $S_\nu$  for field  $i$  as  $f_i(S_\nu)$ , the correction factor per field is simply  $C_i = f_i^{-1}(S_\nu)$ . For multiple fields, we then adopt the full completeness to be

$$C(S_\nu) = \frac{\sum_i f_i^{-1}(S_\nu) \Omega_i(S_\nu)}{\sum_i \Omega_i(S_\nu)}, \quad (1)$$

where  $\Omega_i(S_\nu)$  denotes the area in  $\text{arcmin}^2$  across which a source of flux density  $S_\nu$  can be detected in field  $i$  at  $\geq 3\sigma$  significance. As such, the overall completeness is the area-weighted average of the completeness in the COSMOS and GOODS-N fields.

We present the completeness-corrected Euclidean-normalized number counts at 34 GHz in Figure 7, and tabulate the results in Table 2. The number counts combine the continuum detections across both the COSMOS and GOODS-N fields, using the same area-weighting that is adopted for the completeness calculation (Equation (1)). The uncertainties on the individual points constitute the combination of the error on the counting statistics from Gehrels (1986)—which are more appropriate than simple Poissonian errors for bins with few sources—and the error on the completeness. Cosmic variance is not included in the uncertainties, but its magnitude is discussed below.

While the high-frequency ( $\nu \gtrsim 30$  GHz) radio sky has been explored at the millijansky level (e.g., Mason et al. 2009), the COLDz survey provides the first constraints on the 34 GHz

**Table 2**  
Euclidean Number Counts at 34 GHz

$S_{\text{centre}}$ ( $\mu\text{Jy}$ )	$S_{\text{low}}$ ( $\mu\text{Jy}$ )	$S_{\text{high}}$ ( $\mu\text{Jy}$ )	$n_{\text{uncorr}}(S)$ ( $\text{Jy}^{3/2} \text{sr}^{-1}$ )	$n_{\text{corr}}(S)$ ( $\text{Jy}^{3/2} \text{sr}^{-1}$ )
5.7	3.2	10.1	$0.108^{+0.085}_{-0.051}$	$0.254^{+0.212}_{-0.132}$
17.9	10.1	31.8	$0.514^{+0.235}_{-0.168}$	$0.763^{+0.382}_{-0.274}$
56.6	31.8	100.6	$0.209^{+0.203}_{-0.114}$	$0.209^{+0.203}_{-0.114}$
178.8	100.6	317.8	$0.765^{+1.010}_{-0.494}$	$0.765^{+1.010}_{-0.494}$

**Note.** (1) Central flux density of the bin; (2), (3) lower and upper flux density of the bin; (4) number counts uncorrected for incompleteness; and (5) number counts corrected for incompleteness.

number counts in the regime where star-forming galaxies are expected to emerge as the dominant population, complicating any direct comparisons to the literature. At the bright end of our 34 GHz observations, we compare with Murphy & Chary (2018), who perform a stacking analysis in Planck observations at 28.5 GHz, based on priors at 1.4 GHz from the NRAO VLA Sky Survey (NVSS; Condon et al. 1998). We rescale the number counts from 28.5 to 34 GHz adopting  $\alpha = -0.70$ , and find them to be in agreement with the COLDz observations at  $S_{34} \gtrsim 200 \mu\text{Jy}$ .

As no 34 GHz observations with a similar sensitivity to COLDz exist in the literature, the next best solution is to compare to the highest-frequency number counts available, and scale the counts to 34 GHz. For this, we adopt the recent 10 GHz number counts from van der Vlugt et al. (2021), as part of the COSMOS-XS survey, which we scale to 34 GHz via  $\alpha = -0.70$ . As the parent survey constitutes a very deep single pointing ( $\sim 0.40 \mu\text{Jy}$  across  $\sim 30 \text{ arcmin}^2$ ), these data probe down to slightly fainter flux densities than those probed in this work. However, within the flux density range in common, we find that the number counts are in good agreement, despite the inherent uncertainties associated with the required frequency scaling.

While observationally little is known about the faint high-frequency radio sky, this is no less true for simulations. Modeling of the radio sky has predominantly been performed at low frequencies, with simulations by Wilman et al. (2008) and more recently by Bonaldi et al. (2019) only extending to 18 and 20 GHz, respectively. As such, we again invoke a frequency scaling to 34 GHz, adopting as before a spectral index of  $\alpha = -0.70$ . We focus on the recent 20 GHz simulations by Bonaldi et al. (2019), who model the radio population for two distinct classes of sources: star-forming galaxies that follow the FIRRC, and radio AGNs that show a strong excess in radio power compared to this correlation. We show both the individual and combined contributions of the two populations in Figure 7, and find that the simulations predict that below  $S_{34} \lesssim 100 \mu\text{Jy}$ , star-forming galaxies should make up the bulk of the radio population. Our measurements are in good agreement with the simulated number counts, indicating that a scaling from 20 to 34 GHz with a fixed spectral index is likely to be appropriate. We caution, however, that the uncertainties on our number counts are large as a result of the small number of sources detected in the 34 GHz continuum maps.

Furthermore, cosmic variance constitutes an additional uncertainty on our number counts, as our radio observations probe a relatively small field of view. We show the area probed

as a function of flux density in the bottom panel of Figure 7. Out to  $S_{34} \lesssim 15 \mu\text{Jy}$ , the total area is dominated by the deeper COSMOS mosaic, and accounts for approximately  $10 \text{ arcmin}^2$ . At flux densities above  $S_{34} \gtrsim 30 \mu\text{Jy}$ , our field of view increases to approximately  $60 \text{ arcmin}^2$ , as now sources can be detected across the full GOODS-N mosaic as well. We quantify the magnitude of cosmic variance via the Bonaldi et al. (2019) simulations, following Algera et al. (2020b). Briefly, for each of the flux density bins adopted in our computation of the 34 GHz number counts, we determine the effective area of the COLDz survey in which sources in the given bin can be detected. We then sample 200 independent circular regions of equivalent area from the 20 GHz Bonaldi et al. (2019) simulations, accounting for the flux density scaling with  $\alpha = -0.70$ . We determine the number counts for all independent areas, and compute the 16–84th and 5–95th percentiles, which we adopt to be the  $1\sigma$  and  $2\sigma$  uncertainties due to cosmic variance, shown as the dark and light gray regions in Figure 7, respectively. We note that such a calculation of the cosmic variance encapsulates two effects: at low flux densities, we have a relatively small field of view, which naturally increases the magnitude of cosmic variance. At large flux densities, our field of view constitutes the full  $\sim 60 \text{ arcmin}^2$ , but due to the relative paucity of bright radio sources, cosmic variance similarly constitutes an appreciable uncertainty. The typical magnitude of cosmic variance between  $5 \lesssim S_{34} \lesssim 60 \mu\text{Jy}$  induces an additional uncertainty on the number counts of  $\sim 0.1$ – $0.2$  dex—comparable to the Poissonian uncertainties—although this value rapidly increases for higher flux densities. Overall, we therefore conclude that our number counts are in good agreement with both observed and simulated counts from the literature at lower frequencies.

## 6. 34 GHz Continuum Source Properties

### 6.1. Radio AGNs

In the local universe, the existence of a linear correlation between the total FIR and radio emission of star-forming galaxies has been well established (Yun et al. 2001; Bell 2003). This FIRRC has been shown to hold over a wide range of luminosities, from dwarf galaxies to dust-obscured starbursts (Bell 2003). The correlation is commonly expressed via parameter  $q_{\text{IR}}$ , first introduced by Helou et al. (1985), and defined as

$$q_{\text{IR}} = \log_{10} \left( \frac{L_{\text{IR}}}{3.75 \times 10^{12} \text{ W}} \right) - \log_{10} \left( \frac{L_{1.4}}{\text{W Hz}^{-1}} \right). \quad (2)$$

Here  $L_{\text{IR}}$  represents the 8–1000  $\mu\text{m}$  luminosity, and  $L_{1.4}$  is the  $K$ -corrected radio luminosity at rest-frame 1.4 GHz, computed via the closest observed-frame flux density and the measured radio spectral index. A number of recent, radio-selected studies of the FIRRC have found it to evolve with cosmic time (e.g., Calistro Rivera et al. 2017; Delhaize et al. 2017; Read et al. 2018; Ocran et al. 2020). While the origin of this evolution is debated, and may be the result of residual AGN contamination (Molnár et al. 2018), or due to the different physical conditions in massive star-forming galaxies at high redshift compared to local sources (Algera et al. 2020a; Delvecchio et al. 2021), we adopt an evolving FIRRC to identify radio AGNs among the eighteen 34 GHz detections. In particular, we adopt the correlation determined for a 3 GHz-selected sample by Delhaize et al. (2017), and follow Algera et al. (2020b)

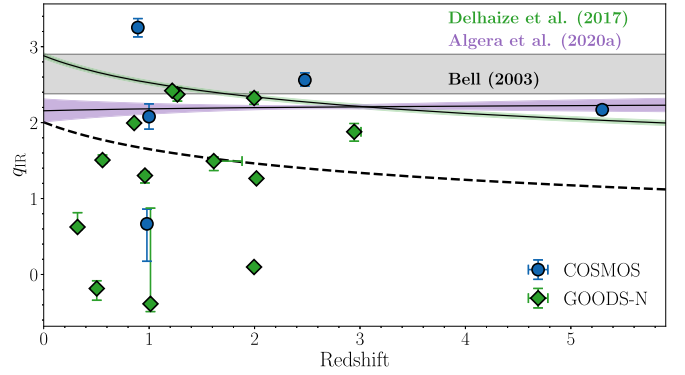


**Figure 8.** The FIRRC for the COLDz 34 GHz continuum detections. Three literature results for the correlation are shown: the local value from Bell (2003), the correlation for 3 GHz-selected galaxies from Delhaize et al. (2017), and the correlation for submillimeter galaxies from Algera et al. (2020a). The threshold for identifying radio-excess AGNs is shown via the dashed curve, which is the FIRRC from Delhaize et al. (2017) minus  $2.5 \times$  the intrinsic scatter. We identify half of the 34 GHz continuum sample (9/18 sources) as radio AGNs.

by identifying galaxies as radio AGNs if they fall below the correlation at the  $2.5\sigma$  level.

We show the FIRRC for the eighteen 34 GHz continuum detections as a function of redshift in Figure 8. In total, half of the COLDz sample are identified as radio AGNs, comprising eight AGNs in GOODS-N, and one in COSMOS (Table 4). The fact that radio AGNs make up a large fraction of the bright radio population is evidenced by the relatively large contribution of AGNs in the wider but shallower GOODS-N observations. Among the galaxies classified as star-forming, Figure 6 suggests the existence of an extended tail at 34 GHz in COLDz-cont-COS-2, at face value indicative of an AGN jet. However, such extended features are absent in the deeper 3 and 10 GHz observations of this source, and at these frequencies, the galaxy is consistent with being a point source at  $2''$  resolution. As the spectrum of jetted AGNs tends to steepen toward higher frequencies (e.g., Mahatma et al. 2018), and should therefore be detectable in the lower-frequency ancillary radio data, we interpret the extended tail at 34 GHz as simply being due to noise. As we adopt the peak brightness for COS-2, its flux density measurement is unlikely to be substantially affected by this noisy region in the radio map.

In total, six out of eight radio AGNs in the GOODS-N field are additionally classified as AGNs through their strong X-ray emission. While constituting only a small number of sources, this is a relatively large fraction, as the overlap between radio AGNs selected at lower frequencies and X-ray AGNs is typically found to be small ( $\lesssim 30\%$ ; e.g., Delvecchio et al. 2017; Smolčić et al. 2017; Algera et al. 2020b). This difference, however, may in part be due to the deeper X-ray data available in GOODS-N, compared to the COSMOS field where these studies were undertaken.

We further show the long-wavelength spectra of the nine radio AGNs in Figure 9. The median 1.4–34 GHz spectral index of the sample equals  $\alpha = -0.77 \pm 0.13$ , which is consistent with the commonly assumed synchrotron slope of  $\alpha = -0.70$ . However, the modest sample still spans a wide range of spectral slopes between 1.4 and 34 GHz, ranging from nearly flat ( $\alpha = -0.04 \pm 0.02$ ) to steep ( $\alpha = -1.47 \pm 0.06$ ). In addition, the AGNs exhibit relatively smooth spectra, with the median spectral index between 1.4–3 (or 5) GHz of  $\alpha_{3/5}^{1.4} = -0.70 \pm 0.12$  being consistent with the typical high-

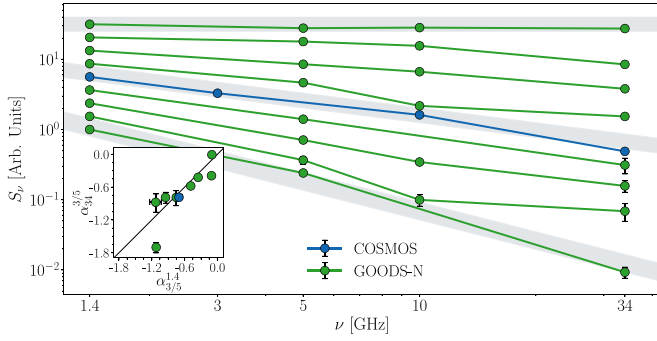


**Figure 9.** The radio spectra of the nine radio AGNs identified in COSMOS (1) and GOODS-North (8). The sources have been arbitrarily normalized, and are arranged from the flattest to steepest 1.4–34 GHz spectral index. Note that the error bars are typically smaller than the chosen plotting symbols. The gray bands indicate slopes of  $\alpha = 0.0$ ,  $-0.70$ , and  $-1.40$  (from top to bottom), comparable to the flattest, median, and steepest 1.4–34 GHz spectral slopes we observe for the COLDz AGNs, and are shown for reference. The inset shows the 5–34 GHz spectral index vs. the 1.4–5 GHz slope (3–34 GHz and 1.4–3 GHz for COSMOS). The radio AGNs show a variety of spectral slopes, with a median spectral index of  $\alpha_{34}^{1.4} = -0.77 \pm 0.13$ . However, the AGNs exhibit relatively smooth radio spectra, with only two sources showing strong evidence for spectral curvature.

frequency slope of  $\alpha_{34}^{3/5} = -0.79 \pm 0.15$ . Only two AGNs exhibit strong evidence for steepening of their radio spectra toward higher frequencies, although sources with strongly steepening spectra are more likely to be missed in a selection at high radio frequencies. Such spectral steepening is expected to occur due to synchrotron aging losses increasing toward higher frequencies, and in turn relates to the age of the AGNs (e.g., Carilli et al. 1991).

### 6.2. Radio Spectral Decomposition for Star-forming Galaxies

Detecting radio FFE in high-redshift star-forming galaxies is challenging due to its expected faintness, and the presence of a radio AGNs only further hinders the detection of this already elusive component in the radio spectrum. As such, we now turn our attention to the star-formation-powered sources detected in the COLDz survey. The radio spectrum of star-forming galaxies is frequently assumed to be the superposition of two power laws arising from nonthermal synchrotron and thermal FFE (Condon 1992; Murphy et al. 2017; Tabatabaei et al. 2017). Denoting their spectral indices as  $\alpha_{\text{NT}}$  and  $\alpha_{\text{FF}}$ , respectively, the radio flux density at a given frequency  $\nu$  may be written as

$$S_\nu = S_{\nu_0}^{\text{NT}} \left( \frac{\nu}{\nu_0} \right)^{\alpha_{\text{NT}}} + S_{\nu_0}^{\text{FF}} \left( \frac{\nu}{\nu_0} \right)^{\alpha_{\text{FF}}}, \quad (3)$$

given a reference frequency  $\nu_0$ , as well as the thermal and nonthermal flux densities  $S_{\nu_0}^{\text{FF}}$  and  $S_{\nu_0}^{\text{NT}}$ , respectively, evaluated at this frequency. We rewrite this equation by introducing the thermal fraction, defined through  $f_{\nu_0}^{\text{th}} = S_{\nu_0}^{\text{FF}} / (S_{\nu_0}^{\text{FF}} + S_{\nu_0}^{\text{NT}})$ , as is common in the literature (e.g., Condon 1992; Tabatabaei et al. 2017). As such, we rewrite the radio spectrum as

$$S_\nu = (1 - f_{\nu_0}^{\text{th}}) S_{\nu_0} \left( \frac{\nu}{\nu_0} \right)^{\alpha_{\text{NT}}} + f_{\nu_0}^{\text{th}} S_{\nu_0} \left( \frac{\nu}{\nu_0} \right)^{-0.1}. \quad (4)$$

This further assumes that the spectral index for thermal FFE is fixed at  $\alpha_{\text{FF}} = -0.10$  (Condon 1992; Murphy et al. 2011). We then determine the remaining free parameters,  $f_{\nu_0}^{\text{th}}$ ,  $\alpha_{\text{NT}}$  and  $S_{\nu_0}$ ,

using a Monte Carlo Markov Chain (MCMC) based fitting routine. In addition, we adopt an observer-frame frequency of 1.4 GHz as the reference frequency  $\nu_0$ , which defines the frequency where the thermal fraction is normalized. Where necessary, we convert the thermal fraction from observed-frame frequency  $\nu$  to a rest-frame frequency  $\nu'$  via

$$f_{\nu'}^{\text{th}} = \frac{f_{\nu(1+z)}^{\text{th}} \left( \frac{\nu'}{\nu(1+z)} \right)^{-0.10}}{f_{\nu(1+z)}^{\text{th}} \left( \frac{\nu'}{\nu(1+z)} \right)^{-0.10} + (1 - f_{\nu(1+z)}^{\text{th}}) \left( \frac{\nu'}{\nu(1+z)} \right)^{\alpha_{\text{NT}}}}. \quad (5)$$

We adopt flat priors in our fitting routine for the normalization  $S_{\nu_0}$  and thermal fraction  $f_{\text{th}}$ , while we adopt Gaussian priors for the nonthermal spectral index (following, e.g., Linden et al. 2020). For the former two parameters, we require that  $-1 \text{ Jy} < S_{\nu_0} < 1 \text{ Jy}$  and  $-0.5 < f_{\text{th}} < 1.5$ , that is, we allow both the normalization and the thermal fraction to take on unphysical, negative values, as artificially bounding both to be greater than zero will not fully capture the uncertainties in the MCMC sampling. In addition, allowing negative values in the thermal fraction will demonstrate the necessity for the thermal component, as well as limitations inherent to the simple model we adopt for the radio spectrum (see also Tabatabaei et al. 2017).

The Gaussian priors adopted on the nonthermal spectral index are motivated by a degeneracy that manifests between the synchrotron slope and thermal fraction at low signal-to-noise. This degeneracy occurs because it is impossible to accurately distinguish between an overall flat spectrum as being due to dominant FFE, or an intrinsically shallow synchrotron slope. To partially alleviate this degeneracy, we adopt prior knowledge from the local universe that the synchrotron spectral indices are typically distributed around  $\alpha_{\text{NT}} \approx -0.85$  (Niklas et al. 1997; Murphy et al. 2011). In large radio-selected samples, the scatter around the typical low-frequency spectral index equals 0.3–0.5 dex (Calistro Rivera et al. 2017; Smolčić et al. 2017; Gim et al. 2019), and is approximately Gaussian. While these spectral index measurements include both the synchrotron and free-free components, the low-frequency nature of these data ensure the radio fluxes are likely dominated by nonthermal emission, and as such, the overall variation in the spectral index constitutes a proxy for the scatter in the typical synchrotron spectral index. To encompass the full observed scatter in the synchrotron slopes, we therefore adopt a Gaussian prior on  $\alpha_{\text{NT}}$  centered on a mean value of  $-0.85$ , with a scatter of 0.50.

### 6.3. Line and Dust Continuum Subtraction

Prior to fitting the radio spectra of the star-forming COLDz continuum detections, we need to ensure the 34 GHz flux density is not contaminated by thermal emission from dust, or by strong line emission. In particular, the 34 GHz flux density of the two COLDz COSMOS sources detected in CO-emission (COS-2, a.k.a. AzTEC.3, and COS-4), may be boosted by their respective CO-lines. We re-extract the peak brightness of these two sources after removing the channels contaminated by the CO-emission, and, as a sanity check, repeat this for the three COSMOS sources that do not show any evidence for strong line emission. While for the latter, the flux densities are

unaffected by this procedure, we find line-uncontaminated flux densities for COS-2 and COS-4 of  $S_{34} = 5.2 \pm 1.3 \mu\text{Jy}$  and  $S_{34} = 3.0 \pm 1.4 \mu\text{Jy}$ , respectively, which are lower than the original cataloged flux densities by  $\sim 25\%$  and  $\sim 40\%$  (Table 1). In turn, this correction brings the 34 GHz flux density from COS-4 below the formal detection limit ( $S/N \approx 2$ ).

The 34 GHz continuum flux densities may further contain a contribution from thermal emission by dust, which, at least for local normal star-forming galaxies, is thought to dominate the radio spectrum beyond rest-frame  $\nu \gtrsim 100\text{--}200$  GHz (Condon 1992). To determine the extent of this contribution, we fit—where available—the FIR observations of our galaxy sample with both optically thin and thick modified blackbody spectra, and extrapolate the resulting dust SED to observed-frame 34 GHz. We note that this methodology is rather sensitive to how well the global dust properties (e.g., temperature and emissivity) can be constrained, and as a result the predicted flux densities are quite uncertain. Nevertheless, we find that the 34 GHz emission of COS-2 and COS-4 is likely to be dominated by emission from dust, with predicted dust contributions of  $4.9^{+6.1}_{-3.6} \mu\text{Jy}$  and  $3.3^{+7.2}_{-1.5} \mu\text{Jy}$ , respectively. As a result, the full 34 GHz flux densities of these two sources are consistent with being powered by the combination of CO-emission and dust. As we probe rest-frame frequencies of  $\nu' \approx 210$  GHz and  $\nu' \approx 120$  GHz for COS-2 and COS-4, respectively, this finding is consistent with the typical model for the long-wavelength SED of star-forming galaxies (Condon 1992).

In what follows, we will discard COS-2 and COS-4 from our sample, as any remaining contribution from free-free or synchrotron emission to the measured 34 GHz flux density is not statistically significant, such that no robust spectral decomposition for these two sources can be performed. One source in GOODS-N, GN-7 at  $z = 2.95$  ( $\nu' \approx 130$  GHz), may have  $\sim 25\%$  of its continuum flux density contaminated by dust emission. However, due to the aforementioned uncertainties in the fitting of the dust SED, we do not correct for this potential contribution. This analysis indicates that, even at low flux densities ( $S_{34} \lesssim 25 \mu\text{Jy}$ ), a 34 GHz-selected sample does not automatically yield a free-free-dominated population.

#### 6.4. The Radio Spectra of High-redshift Star-forming Galaxies

We show the radio spectra of the seven remaining star-forming sources across the COSMOS and GOODS-N fields in Figure 10. All sources can be well described by the combination of a synchrotron and free-free component, although for three sources (COS-5, GN-7, and GN-11)—while some contribution from FFE is preferred—the fitted thermal fractions are consistent with zero within  $1\sigma$ . In turn, for these sources, a single power law representing synchrotron emission is sufficient to match the observed flux densities. We additionally emphasize that there is considerable covariance between the thermal fraction and synchrotron slope, and as such, any quoted 1D uncertainties are not fully representative of the multidimensional posterior distribution (Figure 11). We therefore utilize these full posterior distributions in order to propagate the uncertainties into physical quantities such as free-free SFRs (Section 6.5).

The fitted spectral parameters are presented in Figure 11 and Table 3. Our bootstrapped median thermal fraction, scaled to 1.4 GHz rest frame as is common in the literature, equals  $f_{\text{th}} = 0.06 \pm 0.03$ , with a standard deviation of  $\sigma = 0.05$ . None of the seven star-forming galaxies exhibit thermal fractions of

$f_{\text{th}} \gtrsim 0.20$ , indicating a fairly narrow distribution of  $f_{\text{th}}$  at rest-frame 1.4 GHz, even among a sample showing substantial variation in SFRs. Our average thermal fraction is slightly lower than the average value observed by Tabatabaei et al. (2017) of  $f_{\text{th}} = 0.10$  for star-forming galaxies in the local universe, though they report a large scatter of  $\sigma = 0.09$ . Additionally, the typical thermal fraction is similar to what was observed by Niklas et al. (1997), who determined  $f_{\text{th}} = 0.08 \pm 0.01$  at 1 GHz, with a scatter of  $\sigma = 0.04$  across 74 local galaxies.

We further determine an average thermal fraction at observed-frame 34 GHz (i.e., probing  $34 \times (1+z)$  GHz rest frame) of  $f_{\text{th}} = 0.78 \pm 0.07$ , with a range of  $f_{\text{th}} = 0.45\text{--}0.95$ , and a scatter of  $\sigma = 0.20$  (Figure 12). As such, we find that, even at rest-frame frequencies  $\nu \gtrsim 60$  GHz, the radio spectrum is not fully dominated by thermal FFE, though we caution that the uncertainties on the individual thermal fractions are large. We first compare these results with two local studies, both of which map FFE on subkiloparsec scales. At a typical resolution of  $\approx 0.9$  kpc, Murphy et al. (2012) find an average thermal fraction across 103 star-forming regions of  $f_{\text{th}} = 0.76$  at rest-frame 33 GHz, with a scatter of  $\sigma = 0.24$ . Extrapolating this value via the simple model from Condon (1992), the typical thermal fraction at  $\sim 60$  GHz is expected to be  $\sim 0.85\text{--}0.90$ , which is slightly higher than the thermal fraction we find for high-redshift star-forming galaxies. In addition, Linden et al. (2020) recently measured a typical thermal fraction at 33 GHz of  $f_{\text{th}} = 93 \pm 0.8\%$  across 118 star-forming complexes in local galaxies, at a resolution of  $\approx 0.2$  kpc. Their typical thermal fraction is both higher than that determined by Murphy et al. (2012) and the values measured in this work. This, however, is not surprising, given that the thermal fractions presented in this work are integrated over the entire galaxy. As FFE is predominantly produced in star-forming regions, spatial variations in the thermal fraction across a galaxy are naturally expected, with the thermal fraction peaking in star-forming complexes.

At high redshift, no previous studies have directly targeted the free-free-dominated regime ( $\nu \gtrsim 30$  GHz) in blindly selected galaxy samples, at a depth where star-forming galaxies are expected to dominate the radio population. However, particularly in bright dusty star-forming galaxies, some works have serendipitously detected high-frequency radio continuum emission, typically as a byproduct when targeting the CO(1-0) line. Thomson et al. (2012) detect FFE in two  $z \sim 2.9$  lensed submillimeter galaxies, and determine thermal fractions of  $f_{\text{th}} \sim 0.3\text{--}0.4$  at 34 GHz. Other studies of highly star-forming galaxies (Aravena et al. 2013; Huynh et al. 2017) have additionally detected radio continuum emission at observed-frame  $\sim 30\text{--}35$  GHz, but had to assume fixed synchrotron spectral indices due to a lack of ancillary data. Nevertheless, they estimate thermal fractions between  $f_{\text{th}} \sim 40\%\text{--}70\%$ . Overall, these studies find thermal fractions that are broadly consistent with, albeit typically slightly lower than, what we determine for the star-forming sample detected in our non-targeted 34 GHz observations.

Finally, we compare our results with the 10 GHz pointing from Murphy et al. (2017) in GOODS-N. They determine thermal fractions from 1.4–10 GHz spectral indices for  $\sim 25$  galaxies, under the assumption of a fixed synchrotron slope of  $\alpha_{\text{NT}} = -0.85$ . At a typical rest-frame frequency of  $\nu \sim 20$  GHz, they find a median thermal fraction of  $f_{\text{th}} \approx 50\%$ . Extrapolating

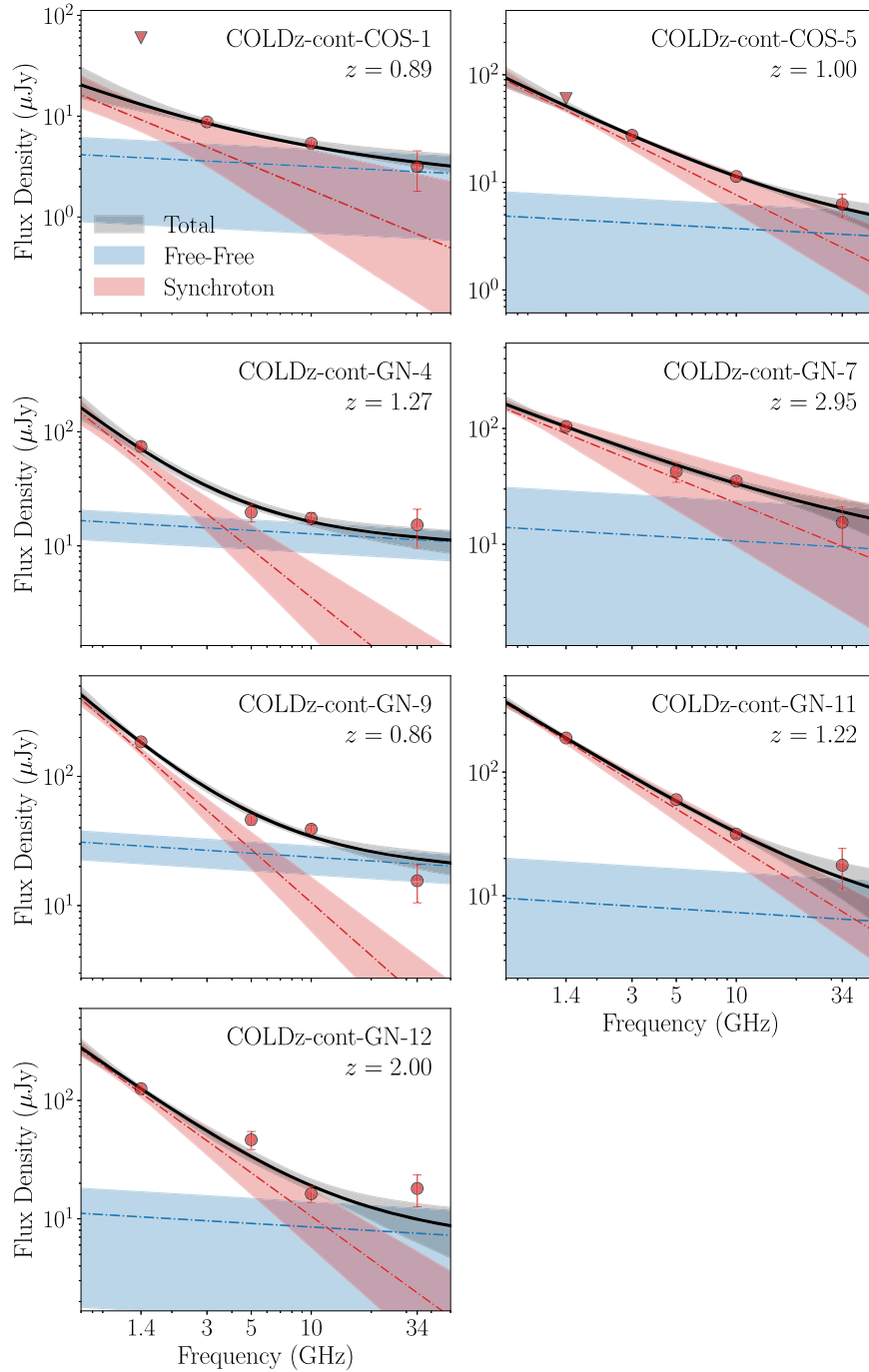


**Figure 10.** The radio spectra of the seven star-forming galaxies in the COSMOS (first two panels) and GOODS-North (last five) fields. We show the decomposition of the spectra into their synchrotron and free-free components, with the shaded regions indicating the  $1\sigma$  confidence region on the fits. We find the radio emission for four out of seven galaxies (COS-1, GN-4, GN-9, and GN-12) to be dominated by free-free emission at observed-frame 34 GHz, whereas for the remainder, only a relatively minor thermal contribution is preferred.

this value to rest-frame 60 GHz, this would imply a thermal fraction of  $f_{\text{th}} \sim 0.7$ , similar to what we observe among the COLDz star-forming sample.

We further determine a median nonthermal spectral index for the star-forming COLDz sample of  $\alpha_{\text{NT}} = -0.99^{+0.19}_{-0.37}$ , with a standard deviation of  $\sigma = 0.25$ . This typical value is consistent with the value observed by Tabatabaei et al. (2017) for local star-forming galaxies of  $\alpha_{\text{NT}} = -0.97 \pm 0.16$ , but is slightly steeper than that of individual star-forming regions in NGC 6946, where Murphy et al. (2011) find a typical value of  $\alpha_{\text{NT}} = -0.81 \pm 0.02$ . This is not surprising, as these observations directly target the

acceleration sites of cosmic rays, where the spectrum should be flatter. However, our median synchrotron slope is additionally slightly steeper than the value obtained by Niklas et al. (1997), who determine an average  $\alpha_{\text{NT}} = -0.83 \pm 0.02$  ( $\sigma = 0.13$ ) across 74 local galaxies. The slightly steeper nonthermal spectral index we find for the COLDz sample may be the result of the higher rest-frame frequencies probed in this work, compared to the aforementioned local studies. Synchrotron cooling losses increase toward high rest-frame frequencies, and result in the steepening of the nonthermal spectral index (e.g., Thomson et al. 2019). While our data do not have the constraining power to determine whether

**Table 3**  
Spectral Parameters of the Star-forming COLDz Sample

ID	$\nu'^a$ (GHz)	$f_{\text{th}}(1.4 \text{ GHz})^b$	$f_{\text{th}}(\nu')^c$	$\alpha_{\text{NT}}$	$\text{SFR}_{\text{FF}}^d$ ( $\log M_{\odot} \text{ yr}^{-1}$ )	$\text{SFR}_{1.4}$ ( $\log M_{\odot} \text{ yr}^{-1}$ )
COLDz-cont-COS-1	64	$0.18^{+0.11}_{-0.15}$	$0.82^{+0.14}_{-0.71}$	$-0.81^{+0.38}_{-0.49}$	$28^{+19}_{-23}$	$12^{+2}_{-2}$
COLDz-cont-COS-5	68	$0.05^{+0.02}_{-0.05}$	$0.60^{+0.22}_{-0.61}$	$-0.94^{+0.22}_{-0.21}$	$53^{+20}_{-54}$	$69^{+5}_{-5}$
COLDz-cont-GN-4	77	$0.08^{+0.03}_{-0.02}$	$0.95^{+0.04}_{-0.14}$	$-1.40^{+0.33}_{-0.36}$	$289^{+123}_{-94}$	$213^{+47}_{-40}$
COLDz-cont-GN-7	134	$0.06^{+0.04}_{-0.13}$	$0.50^{+0.38}_{-1.20}$	$-0.71^{+0.23}_{-0.34}$	$1440^{+1181}_{-3530}$	$857^{+239}_{-161}$
COLDz-cont-GN-9	63	$0.08^{+0.01}_{-0.02}$	$0.91^{+0.05}_{-0.12}$	$-1.36^{+0.21}_{-0.25}$	$254^{+45}_{-32}$	$254^{+19}_{-18}$
COLDz-cont-GN-11	75	$0.02^{+0.02}_{-0.03}$	$0.45^{+0.30}_{-0.74}$	$-0.99^{+0.13}_{-0.15}$	$162^{+166}_{-243}$	$444^{+34}_{-32}$
COLDz-cont-GN-12	102	$0.02^{+0.01}_{-0.02}$	$0.78^{+0.16}_{-0.53}$	$-1.22^{+0.24}_{-0.28}$	$342^{+174}_{-260}$	$622^{+127}_{-96}$

**Notes.**

<sup>a</sup> The rest-frame frequency probed by the COLDz 34 GHz observations.

<sup>b</sup> The thermal fraction at rest-frame 1.4 GHz.

<sup>c</sup> The thermal fraction at rest-frame frequency  $\nu'$ .

<sup>d</sup> The uncertainties on the free-free SFRs are propagated from those on the thermal fraction and radio luminosity. The sources where these SFRs are consistent with zero within  $1\sigma$  are plotted as upper limits in Figure 13.

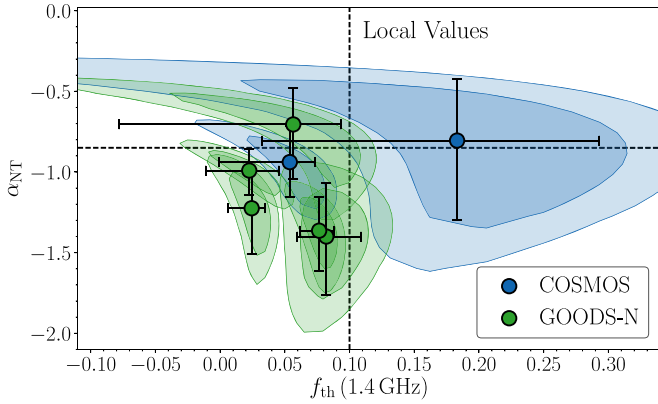


**Figure 11.** The fitted synchrotron spectral index vs. the rest-frame 1.4 GHz thermal fraction for the seven star-forming COLDz continuum detections. The blue and green shaded regions indicate the covariance between the parameters, with the darker (lighter) shading indicating the  $1\sigma$  ( $2\sigma$ ) confidence regions. The data points show the corresponding  $1\sigma$  uncertainties, and the typical local values are indicated through the dashed lines. The COLDz galaxies are predominantly located in the lower left quadrant, indicating slightly steeper synchrotron spectral indices, and lower thermal fractions than what is typically observed locally.

such spectral aging occurs, as this requires additional sampling of the radio spectrum, such increased high-frequency losses would be fitted by a relatively steep synchrotron slope in our two-component model, and may plausibly contribute to our moderately lower value for  $\alpha_{\text{NT}}$  compared to local studies.

Based on the spectral parameters we determine for the COLDz sample, we calculate the rest-frame frequency  $\nu_{50}'$  where the thermal fraction reaches 50% via

$$\nu_{50}' = \nu' \left( \frac{1 - f_{\text{th}}(\nu')}{f_{\text{th}}(\nu')} \right)^{-1/(\alpha_{\text{NT}} + 0.10)} \quad (6)$$

While the uncertainties on this value are substantial for the individual star-forming galaxies due to its dependence on both the thermal fraction and synchrotron slope, we determine a median value of  $\nu_{50}' = 11.5^{+20.0}_{-7.4}$  GHz, with a standard deviation of  $\sigma = 5.9$  GHz. This is slightly lower than, albeit still consistent with, the canonically assumed value of  $\nu_{50}' \approx 25 - 30$  GHz (e.g., Condon 1992), which is likely

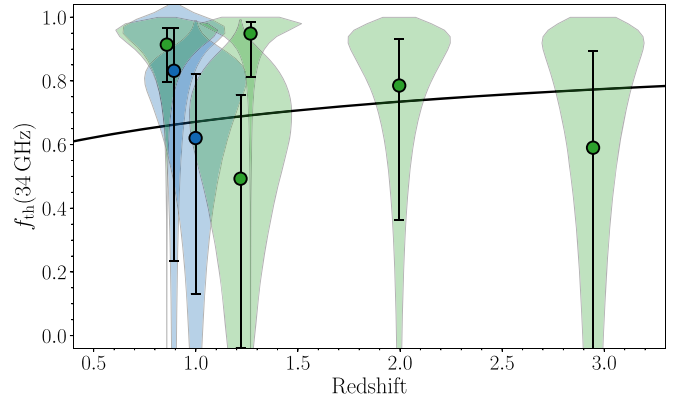


**Figure 12.** Violin diagrams of the thermal fraction at 34 GHz (observed-frame, hence probing rest-frame  $34 \times (1+z)$  GHz) as a function of redshift. The width of the shaded regions represents the probability distribution of the thermal fraction, while the data points indicate the median and 16–84th percentiles. The probability distributions of the thermal fractions are characterized by a typically high probability of having a large thermal fraction  $f_{\text{th}} \gtrsim 0.7 - 0.8$ , with a long tail extending toward lower values. The model from Condon (1992), adopting  $\alpha_{\text{NT}} = -0.85$  and  $f_{\text{th}} = 0.10$  at 1.4 GHz, is shown as the solid black line, and predicts similar high-frequency thermal fractions as observed across the star-forming galaxies.

due to the relatively steep synchrotron slopes we are finding for the COLDz star-forming galaxies.

While the differences between the spectral parameters determined for COLDz and those observed in local star-forming galaxies are of minor statistical significance, a high-frequency selection of star-forming galaxies is likely to bias the sample toward having overall shallow radio spectra. Combining the 10–34 GHz spectral indices for the star-forming galaxies across COSMOS and GOODS-N, we find an average slope of  $\alpha_{34}^{10} = -0.47 \pm 0.10$  ( $\sigma = 0.28$ ), which is substantially shallower than the canonical  $\alpha = -0.70$  assumed at lower frequencies. Shallow spectra are naturally expected in the free-free dominated regime, in particular for young starburst galaxies. Such sources should exhibit large thermal fractions, as synchrotron emission lags the onset of a starburst by  $\gtrsim 30$  Myr (e.g., Bressan et al. 2002), and the galaxies should hence be dominated by FFE across the entire radio spectrum. However, our sample is fully comprised of sources with typical or low thermal fractions ( $f_{\text{th}} \lesssim 0.20$  at 1.4 GHz), and rather steep

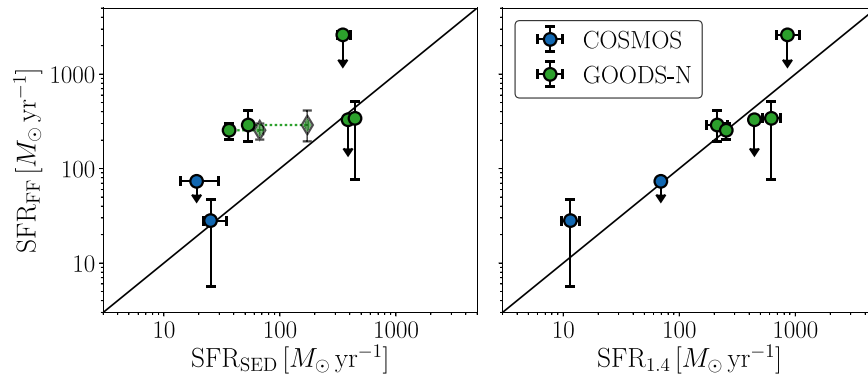


**Figure 13.** Left: a comparison of the star formation rates obtained from free-free emission, vs. those from MAGPHYS. The one-to-one relation is shown through the solid black line, and the vertical error bars represent the propagated uncertainties on the radio luminosity and thermal fraction. For three sources, we can only place upper limits on their free-free SFRs. The diamonds show the SFRs that we infer from SED-fitting when we instead convert the FIR luminosity into a star formation rate, for the two sources where these values are discrepant (see the text for details). Right: free-free star formation rates vs. those obtained from radio synchrotron emission, adopting the FIRRC from Delhaize et al. (2017). Despite the uncertainties on  $\text{SFR}_{\text{FF}}$  being large as a result of the low signal-to-noise at 34 GHz, and the limited available sample size, we find that the free-free star formation rates are in reasonable agreement with the values derived from SED-fitting and low-frequency radio emission.

synchrotron spectra ( $\alpha_{\text{NT}} \lesssim -0.85$ ). This, in turn, indicates we are likely detecting relatively mature starbursts, as opposed to young star-forming galaxies. In particular, galaxies with a declining star formation history are expected to exhibit only modest levels of FFE at low radio frequencies, and may show steepening of their synchrotron spectra toward higher frequencies. This scenario is qualitatively consistent with the spectral parameters we are finding for the COLDz star-forming galaxies, and may therefore be typical for a high-frequency-selected sample.

Alternatively, the relatively low thermal fractions observed for our star-forming sample at low frequencies may be the result of residual AGN contamination. An AGN will contribute additional synchrotron emission in excess of that arising from star formation, while the overall contribution from FFE is mostly unaffected. In this case, one may expect typical synchrotron spectra, in combination with low thermal fractions. However, we find no strong evidence for systematic residual radio AGN activity based on the values of  $q_{\text{IR}}$  of our star-forming galaxies, as we find that half of our sample falls onto or above the FIRRC for star-forming galaxies (Delhaize et al. 2017; Algera et al. 2020a).

### 6.5. Free-Free Star Formation Rates

Free-free emission is one of the most robust tracers of star formation, as it constitutes a direct probe of the ionizing photons emitted by recently formed ( $\lesssim 10$  Myr) massive stars. As such, it does not rely on reprocessed starlight, or emission produced by stellar remnants, such as, respectively, FIR and radio synchrotron emission. However, some caveats still apply, as carefully summarized in Querejeta et al. (2019). In particular, any ionizing photons absorbed by dust within the H II region will not contribute to the ionization of hydrogen atoms, and as such will reduce the free-free luminosity at a fixed SFR (e.g., Inoue et al. 2001; Dopita et al. 2003). Alternatively, if there is substantial leakage of ionizing photons, FFE will similarly be suppressed. Finally, since FFE is only sensitive to the massive end of the initial mass function, any variations in the IMF may substantially affect the calculated SFRs. We note that these caveats also apply to SFRs estimated using the Balmer lines (e.g.,  $\text{H}\alpha$ ,  $\text{H}\beta$ ), with the

clear advantage of FFE being that it is fully dust-insensitive on scales beyond the H II region wherein the star formation occurs.

With these caveats in mind, we now set out to calculate free-free SFRs for the seven star-forming galaxies detected at 34 GHz. The calibration from Murphy et al. (2012), adapted to a Chabrier IMF, is given by

$$\left( \frac{\text{SFR}_{\text{FF}}}{M_{\odot} \text{ yr}^{-1}} \right) = 4.3 \times 10^{-28} \left( \frac{T_e}{10^4 \text{ K}} \right)^{-0.45} \left( \frac{\nu}{\text{GHz}} \right)^{0.10} \times \left( \frac{f_{\text{th}}(\nu) L_{\nu}}{\text{erg s}^{-1} \text{ Hz}^{-1}} \right). \quad (7)$$

Here  $T_e$  is the electron temperature, which we assume to equal  $T_e = 10^4$  K. However, we note that our results are somewhat insensitive to the precise value adopted, given the modest exponent of  $T_e^{-0.45}$ . The SFR is further directly proportional to the product of the thermal fraction and the radio luminosity, which we evaluate at a rest-frame frequency of  $\nu = 1.4$  GHz.

We derive typical free-free SFRs between  $\text{SFR} \approx 30$ – $350 M_{\odot} \text{ yr}^{-1}$  for the four out of seven sources for which we have robustly constrained thermal fractions. The remaining sources instead have a thermal fraction that is consistent with zero within  $1\sigma$ , such that we can only provide upper limits on their free-free SFRs. We compare the free-free SFRs with those derived from MAGPHYS, as well as from low-frequency radio synchrotron emission in Figure 13. For the latter, we adopt the FIRRC from Delhaize et al. (2017), which is suitable for the radio-detected star-forming population. While we have derived individual  $q_{\text{IR}}$ -values for the star-forming COLDz sample in Section 4, we adopt a fixed FIRRC from the literature to ensure that the synchrotron-derived SFRs are independent of those from FIR emission.

Overall, we observe a reasonable agreement between the SFRs from FFE, and those from the more commonly adopted tracers we use for comparison. This likely implies that the various aforementioned caveats do not greatly affect our calculated SFRs. However, the correlation between the two radio-based tracers appears tighter than the one between the SFRs from FFE and SED-fitting, which is surprising, as the timescale for FIR emission should more closely resemble that of FFE than synchrotron emission. Two sources in particular,

GN-4 ( $z = 1.27$ ) and GN-9 ( $z = 0.87$ ) appear to have well-constrained free-free SFRs that exceed the ones from SED-fitting by a factor of  $5.6 \pm 0.1$  and  $7.0 \pm 0.3$ , respectively. If dust extinction within the H II region, or leakage of ionizing photons were a concern, the free-free SFRs should be suppressed, in contrast to what we observe for these two sources. Instead, for GN-4, this offset is likely related to the SFR determined from SED-fitting. While the infrared SED of this galaxy is well constrained (Figure 17), MAGPHYS predicts that a substantial fraction of the infrared emission from GN-4 originates from an older stellar population, with the ratio between its infrared-based SFR—assuming the conversion from Kennicutt (1998) adjusted for a Chabrier IMF—and the fitted SFR equaling  $3.2 \pm 0.1$ . Given that the SFRs from FFE and the 1.4 GHz luminosity are in good agreement for GN-4, it is likely that the contribution from old stars to the FIR luminosity is overestimated in the SED-fitting.

A similar discrepancy can be seen between the free-free and infrared SFRs derived for GN-9. While this source too has a modest contribution to its dust luminosity from older stars, upon accounting for this, its ratio between the free-free and SED-fitted SFRs remains a factor of  $3.8^{+0.1}_{-0.3}$ . Instead, the radio flux densities of this source are likely to be boosted by the emission from an AGN. We find an FIRRC parameter of  $q_{\text{IR}} = 1.99 \pm 0.04$  for GN-9 (Section 6.1), which implies that it lies  $\sim 0.5$  dex below the median value for radio-selected star-forming galaxies at its redshift of  $z = 0.87$  (Delhaize et al. 2017), though still above the threshold we adopt for identifying radio AGNs. Nevertheless, GN-9 is  $\sim 3.5\times$  radio-bright with respect to the median FIRRC, which fully accounts for the difference between its radio and SED-fitted SFRs.

Interestingly, we can only place upper limits on the free-free SFRs for two of the brightest star-forming galaxies in GOODS-N ( $\text{SFR}_{\text{SED}} \sim 400 M_{\odot} \text{ yr}^{-1}$ ), GN-7 and GN-11. While naively these galaxies might be expected to exhibit strong FFE, recent studies of starburst galaxies have found that their radio spectra might steepen toward higher frequencies (Thomson et al. 2019; Tisanić et al. 2019). This may be related either to a deficit in FFE, or to the steepening of their synchrotron spectra. However, these studies were limited to rest-frame frequencies  $\nu \lesssim 20$  GHz, and hence did not probe the regime where FFE is expected to dominate. While our study does directly target this high-frequency regime, with the current sampling of the radio spectrum, we are unable to distinguish between a deficit in FFE, or more complex behavior in the synchrotron emission. Nevertheless, our lack of a robust detection of FFE in these strongly star-forming sources provides support for the existence of more complex radio spectra, which may be constrained by probing their radio emission at intermediate frequencies, using, for example, the VLA K-band (22 GHz).

Taking the aforementioned caveats into account, our derived free-free SFRs are in good agreement with those from SED-fitting and the low-frequency FIRRC. While the uncertainties on the free-free SFRs remain large as a result of the typical faintness of star-forming galaxies at high rest-frame frequencies, our analysis indicates that a deep, 34 GHz-selected sample, supplemented by deep ancillary radio observations, can be used to accurately constrain star formation at high redshift. This, in turn, will be possible for significantly larger galaxy samples in the future, with the increased sensitivity of next-generation radio facilities.

## 7. Free-Free Emission with the SKA and ngVLA

The next large radio telescope to come online is the Square-Kilometer Array Phase 1 (SKA1), with SKA1-Mid set to cover a frequency range of 0.35–15 GHz. As such, observations with the highest-frequency band of the SKA1-Mid (at a central frequency of  $\nu_c = 12.5$  GHz) will start probing the regime where FFE dominates in star-forming galaxies at  $z \gtrsim 1$ . A galaxy with  $\text{SFR} = 10 M_{\odot} \text{ yr}^{-1}$  at  $z = 1$  will have a flux density of approximately  $S_{12.5} \approx 1.5 \mu\text{Jy}$  in this band, assuming the FIRRC from Delhaize et al. (2017), and the calibration between star formation and FFE from Murphy et al. (2012). This, in turn, requires  $\sim 15$ – $20$  hr of telescope time for a  $5\sigma$  detection, based on the SKA1 sensitivity estimates from Braun et al. (2019). In order to robustly probe the FFE in such a modestly star-forming galaxy, additional sampling of its low-frequency radio spectrum is crucial. In particular, for a similar  $5\sigma$  detection at 1.4 and 6.7 GHz, a further  $\sim 10$ – $15$  hr of total telescope time is required. Given the  $\sim 4\times$  larger field of view at 6.7 GHz compared to at 12.5 GHz, a possible observing strategy for the detection of FFE in faint star-forming galaxies is to combine two single SKA1-Mid pointings at 1.4 and 6.7 GHz with a five-pointing mosaic at 12.5 GHz, covering the entire 6.7 GHz field of view. With a total telescope time of  $\sim 100$  hr, this allows for the mapping of FFE in all  $z \gtrsim 1$  star-forming galaxies at  $S_{12.5} \gtrsim 1.5 \mu\text{Jy}$  across an area of  $\sim 120 \text{ arcmin}^2$ . Adopting the Bonaldi et al. (2019) simulations of the radio sky, developed specifically for the SKA1, typical  $\sim 1100$ – $1200$  galaxies are expected at  $S_{12.5} \gtrsim 1.5 \mu\text{Jy}$  within this field of view. In particular, approximately  $\sim 68 \pm 2\%$  ( $\sim 12 \pm 1\%$ ) of this sample is expected to lie at a redshift  $z \geq 1$  ( $z \geq 3$ ), allowing for the robust sampling of the free-free dominated regime. For comparison, the 200 hr VLA COSMOS-XS survey (van der Vlugt et al. 2021), reaches a similar depth to these template SKA1-Mid observations at 3 and 10 GHz, but covers a smaller area of  $\sim 30 \text{ arcmin}^2$ . The increased survey speed of SKA1-Mid, therefore, allows for a  $\gtrsim 8\times$  quicker mapping of FFE up to  $\sim 15$  GHz, compared to the VLA. However, as the frequency coverage of SKA1-Mid is not fully optimized to directly probe the high-frequency radio emission in star-forming galaxies, significant synergy with the VLA remains, as it allows for the extension of the spectral coverage from the SKA1 to higher frequencies.

The ngVLA (Murphy et al. 2018; McKinnon et al. 2019), however, is set to truly transform our understanding of the high-frequency radio spectrum in distant galaxies, and will allow for the usage of FFE as a high-redshift SFR-tracer on an unprecedented scale. The current sensitivity estimates (Butler et al. 2019) indicate that the ngVLA will attain a typical rms of  $\sigma \approx 0.3 \mu\text{Jy beam}^{-1}$  in one hour of band four ( $\nu = 20.5$ – $34.0$  GHz) observations. This, in turn, translates to a  $5\sigma$  detection of a galaxy forming stars at  $100 M_{\odot} \text{ yr}^{-1}$  at  $z = 2.5$ , probing rest-frame 80 GHz, similar to the frequency range probed in this work for  $z \approx 2$  star-forming galaxies. However, with the expected improvement in sensitivity the ngVLA provides over the current VLA, high-redshift sources may more easily be targeted at relatively low observing frequencies, enabling wider surveys while still allowing for the free-free dominated regime to be probed. For example, Barger et al. (2018) propose a survey at 8 GHz (ngVLA band two) to  $0.2 \mu\text{Jy beam}^{-1}$  across a large area of  $1 \text{ deg}^2$ , which requires just an hour per pointing. By adopting a typical wedding cake strategy, deeper observations across a smaller area can further be used to target fainter star-forming galaxies. As an example, a star-forming galaxy of  $\text{SFR} = 25 M_{\odot} \text{ yr}^{-1}$  at  $z = 3$  ( $z = 5$ ) can in

principle be detected at 8 GHz in only  $\sim 3$  hr ( $\sim 15$  hr), modulo, of course, the large uncertainties on the typical thermal fraction in faint, star-forming sources, and the nature of the FIRRC in this population.

## 8. Conclusions

We have presented a deep continuum survey of the high-frequency radio sky with the VLA, which probes the microjansky galaxy population at 34 GHz. This regime has historically remained largely unexplored due to the relatively low survey speed of radio telescopes at these frequencies, as well as the expected faintness of sources. However, the high radio frequencies hold one of the most reliable tracers of star formation, radio FFE, and as such are set to become a key area of study with next-generation radio facilities.

We employ deep observations at 34 GHz from the COLDz project (Pavesi et al. 2018; Riechers et al. 2019, 2020), which cover the well-studied COSMOS (10 arcmin<sup>2</sup>) and GOODS-North (50 arcmin<sup>2</sup>) fields to a typical depth of  $\sim 1.5 \mu\text{Jy beam}^{-1}$  and  $\sim 5.3 \mu\text{Jy beam}^{-1}$ , respectively. We perform source detection on the images down to a liberal  $3\sigma$  detection threshold, aided by deep ancillary radio data across both fields, resulting in the detection of high-frequency continuum emission in 18 galaxies. We cross-match these detections with additional deep radio observations at 1.4, 3, and 10 GHz in the COSMOS field, as well as data at 1.4, 5, and 10 GHz in GOODS-N. In addition, we leverage the wealth of multiwavelength data across both fields to fully sample the SEDs of the galaxies from the X-ray to radio regime. The COLDz continuum sample spans a redshift range of  $z = 0.50\text{--}5.30$ , and lies at a median (mean) redshift of  $z = 1.12^{+0.52}_{-0.15}$  ( $z = 1.55^{+0.41}_{-0.35}$ ). The sample contains six sources at  $z \geq 2$ , and includes the well-studied submillimeter galaxy AzTEC.3 at  $z = 5.3$ . Our main findings are as follows:

1. We present the first constraints on the radio number counts at 34 GHz in the regime where star-forming galaxies dominate the radio population (Figure 7), and find that these are in good agreement with lower-frequency number counts in the literature, both from observations (van der Vlugt et al. 2021) and simulations (Bonaldi et al. 2019).
2. We use the FIRRC to divide the 34 GHz continuum sample into star-forming galaxies and AGNs (Figure 8). In total, half of the sample (nine sources) shows AGN activity at radio wavelengths (Figure 9), while the radio emission of the remainder is consistent with being powered predominantly through star formation. All but one of the faintest galaxies in our sample ( $S_{34} \lesssim 20 \mu\text{Jy}$ ) show radio emission of a star-forming origin, which is qualitatively consistent with the small fraction of radio AGNs found in deep observations at lower frequencies (e.g., Algera et al. 2020b). Two sources, including AzTEC.3 at  $z = 5.3$ , likely have their continuum emission at 34 GHz dominated by thermal emission from dust, leaving 7/18 sources ( $\sim 40\%$ ) of the sample with high-frequency radio continuum emission dominated by the combination of synchrotron and FFE.
3. We use the wealth of ancillary radio data across the COSMOS and GOODS-N fields to construct radio spectra of the star-forming galaxies, covering four frequencies in the range 1.4–34 GHz (Figure 10). We fit the radio spectra with a combination of free–free and

synchrotron emission, and determine thermal fractions and nonthermal spectral indices for our sample (Figures 11 and 12), which are consistent with the values observed in local galaxies. We further determine free–free SFRs for seven star-forming galaxies, and find good agreement with those obtained from SED-fitting and the FIRRC (Figure 13).

With the 34 GHz continuum data from the COLDz survey, we have directly targeted FFE in faint star-forming sources at high redshift. While currently limited to a modest sample, next-generation radio facilities are set to significantly increase the number of galaxies for which the full radio spectrum is constrained, and will transform our understanding of high-frequency radio continuum emission in star-forming galaxies. However, combined with the wealth of ancillary data in the COSMOS and GOODS-N fields, the COLDz observations already allow for a census of FFE in the typical star-forming population via a multifrequency radio stacking analysis, which will be presented in a forthcoming publication (H. S. B. Algera et al. 2021, in preparation).

The authors would like to thank the anonymous referee for the helpful comments on this manuscript. H.S.B.A. would like to thank A. de Graaff and D. Blanco for useful and constructive discussions. The authors thank Chris Carilli and Ian Smail for providing comments on the manuscript, and Fabian Walter for his help in the early stages of this project. The National Radio Astronomy Observatory is a facility of the NSF operated under cooperative agreement by Associated Universities, Inc. H.S.B.A. and J.A.H. acknowledge support of the VIDI research program with project No. 639.042.611, which is (partly) financed by the Netherlands Organization for Scientific Research (NWO). D.R. acknowledges support from the NSF under grant Nos. AST-1614213 and AST-1910107. D.R. also acknowledges support from the Alexander von Humboldt Foundation through a Humboldt Research Fellowship for Experienced Researchers. M.A. and this work have been supported by grants “CONICYT + PCI + REDES 19019” and “CONICYT + PCI + INSTITUTO MAX PLANCK DE ASTRONOMIA MPG190030.”

## Appendix A Image Properties

We discuss some of the properties of the COSMOS and GOODS-N 34 GHz images below, including the completeness, and the level of flux boosting. In addition, we detail how we assign flux densities to the 34 GHz continuum detections.

### A.1. Completeness

We determine the completeness of the COSMOS and GOODS-N mosaics by inserting mock sources into the image, and extracting them via our regular source detection procedure (Section 3). The fraction of resolved sources at a resolution of  $\sim 2''$  at 10 GHz—similar to the resolution of our 34 GHz observations—is just  $\sim 10\%$  (van der Vlugt et al. 2021), and is expected to be smaller at even higher frequencies, where sources are more compact (Murphy et al. 2017; Thomson et al. 2019). As such, we only include unresolved mock sources in our completeness analysis. Sources are inserted in the maps uncorrected for the primary beam (PB), as in this case, it is straightforward to incorporate the incompleteness due to the decreased PB-sensitivity by inserting sources with a true flux

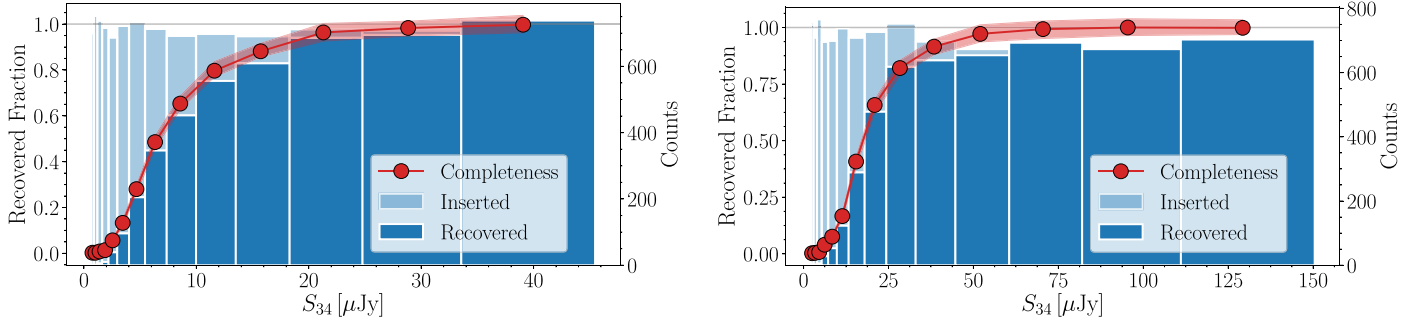


**Figure 14.** Left: completeness analysis for the COSMOS field, showing the fraction of inserted mock sources we recover as a function of their flux density. The red data points and shaded region indicate the measured completeness and confidence region, respectively. Right: completeness analysis for GOODS-North. Both panels take into account the variation in the primary beam sensitivity across the mosaic, and as such, the total completeness correction constitutes the combination of missing sources due to a decreased primary beam sensitivity, and local noise properties within the mosaics.

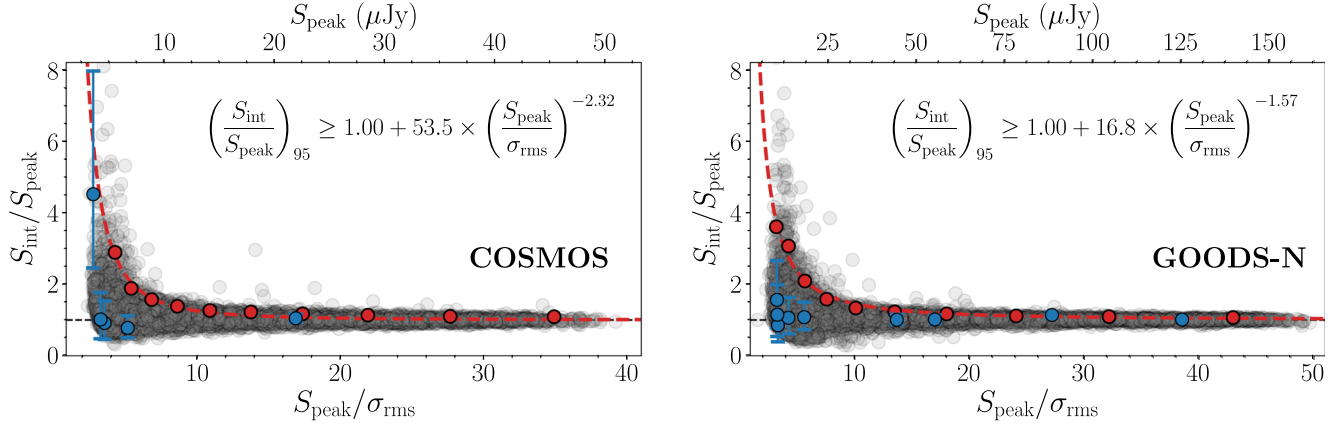


**Figure 15.** The ratio of integrated to peak flux density as a function of the peak S/N for unresolved mock sources inserted into the COSMOS and GOODS-N fields. Both panels show a power-law fit to the upper 95th percentile of each bin in S/N (red points) via the red, dashed line. Sources below this line are taken to be unresolved, and for these, the peak brightness is adopted. The robust sources detected in both fields are shown in blue. A single source in GOODS-N is consistent with being resolved, whereas the remaining continuum detections are unresolved. Since the mock sources are inserted into the mosaic uncorrected for the primary beam, the rms is highly uniform, and hence the S/N can be mapped into a peak brightness (upper horizontal axis).

density  $S_\nu$  as  $A(r) \times S_\nu$ , where  $A(r)$  represents the primary beam sensitivity at position  $r$  within the mosaic.

We randomize source positions within both mosaics, above  $A(r) \geq 0.20$ , and draw flux densities from a power-law distribution to ensure low flux densities—where incompleteness will be the largest—are amply sampled. For COSMOS, we insert 50 mock sources in each run, for a total of 200 runs. As the GOODS-N mosaic is substantially larger, we instead insert 100 mock sources per run, for 100 runs total. In both cases, mock sources are required to be 2.5 beam sizes away from both real sources and other mock sources. We then repeat the source detection procedure described in Section 3, and cross-match the recovered sources to the inserted ones, using a matching radius of  $0''.7$ . We record their inserted flux density, as well as their recovered peak and integrated flux densities. We define the completeness in a given flux density bin  $i$  as  $C_i = N_{\text{rec},i}/N_{\text{ins},i}$ , that is, as the ratio of the number of inserted and recovered mock sources with a flux density that falls within the  $i$ th bin. We determine the corresponding uncertainty via a bootstrap analysis, whereby we resample from the inserted flux densities, with replacement, and determine for each flux density bin the fraction of this sample that was recovered in our source detection procedure. The uncertainty then represents the 16th–84th percentile of the bootstrapped completeness analyses. We show the completeness in both the COSMOS and GOODS-N mosaics in Figure 14.

In the COSMOS field, we reach 50% and 80% completeness at flux densities of  $S_{34} = 7.3 \mu\text{Jy beam}^{-1}$  ( $\approx 6\sigma$ , where  $\sigma$  represents the typical rms in the map) and  $S_{34} = 13.3 \mu\text{Jy beam}^{-1}$  ( $\approx 10\sigma$ ), respectively. In GOODS-North, we reach completeness fractions of 50% and 80% at  $S_{34} = 19.6 \mu\text{Jy beam}^{-1}$  ( $\approx 4\sigma$ ) and  $S_{34} = 29.3 \mu\text{Jy beam}^{-1}$  ( $\approx 6\sigma$ ), respectively. These differences may be explained by the nonuniform exposure map of the GOODS-N mosaic, allowing for faint sources to still be detected in a small portion of the mosaic.

## A.2. Peak versus Integrated Fluxes

In order to assign a flux density to the detected radio sources, we need to establish if they are resolved. Our observations have a typical beam size of  $\sim 2''.5$ , and as such, we expect most sources to be unresolved, based on the typical (sub-)arcsecond radio sizes of star-forming galaxies at low frequencies (Cotton et al. 2018; Jiménez-Andrade et al. 2019), and the finding that these sources are more compact at higher frequencies (Murphy et al. 2017; Thomson et al. 2019). To verify this, we use our runs of inserted mock sources, which, by construction, are unresolved, and compare their peak and integrated flux densities as a function of signal-to-noise. We show the results in Figure 15, for both the COSMOS and GOODS-N fields. We divide the results into logarithmically spaced bins in S/N, and determine the integrated/peak ratio encompassing 95% of sources per bin (following, e.g.,

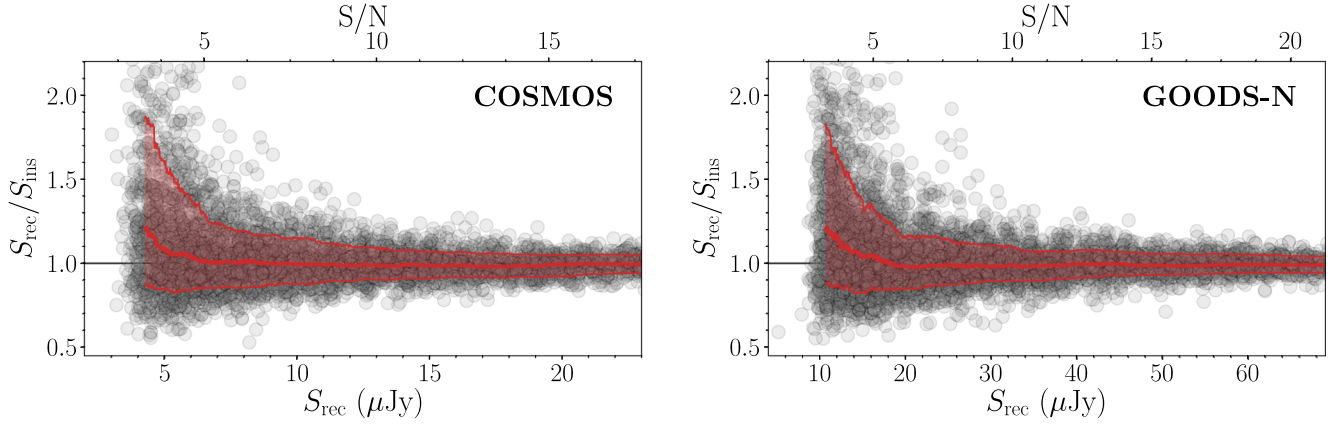


**Figure 16.** The ratio of recovered and inserted peak flux density as a function of recovered flux density, for unresolved mock sources inserted into the COSMOS and GOODS-N 34 GHz maps. A running median and the corresponding 16th–84th percentile spread are indicated through the red line and shaded area, respectively. While for both fields the median level of flux boosting is negligible at  $S/N \gtrsim 5$ , the correction reaches  $\sim 20\%$  at  $S/N \approx 3$ .

Bondi et al. 2008; van der Vlugt et al. 2021). These percentiles are fitted with a power law, with the region below the best fit defining the limiting integrated/peak flux density where sources are taken to be unresolved. It is clear that at a modest signal-to-noise,  $S/N \lesssim 5$ , sources can have  $S_{\text{int}}/S_{\text{peak}} \gtrsim 2$ , despite being unresolved. This is a result of nearby noise peaks elongating the source, or throwing off the fitting, which mostly affects the integrated flux density. We find that all sources, with the exception of one bright ( $S/N \sim 25$ ) detection in GOODS-N, show an integrated/peak ratio that is consistent with the source being unresolved. As such, we adopt the integrated flux density for this single source, and the peak brightness for the rest.

### A.3. Flux Boosting

At low signal-to-noise, the peak brightness may be “boosted” as a result of noise properties in the image. To

establish whether this is affecting the flux densities of our 34 GHz detections, we compare the recovered and inserted flux densities of our mock source analysis. The results are shown in Figure 16, for both COSMOS and GOODS-N. At  $S/N \gtrsim 5$ , the median ratio of recovered-to-inserted flux density is consistent with unity, with a spread of less than  $\lesssim 20\%$ . At  $S/N \lesssim 5$ , which is the typical signal-to-noise at which the faintest 34 GHz sources are detected, the level of flux boosting steadily increases, with a typical correction of  $\sim 20\%$  at  $S/N \approx 3$  in either field. In this low- $S/N$  regime, the typical spread on the ratio of recovered and inserted flux densities similarly increases strongly. Following, e.g., Stach et al. (2019), we correct the flux densities of the sources detected at 34 GHz by the median level of flux boosting at their observed  $S/N$ . The uncertainty on the corrected flux density includes the propagated bootstrapped error on the median.

## Appendix B

### Spectral Energy Distributions

We show the full SEDs for the 18 COLDz continuum detections, fitted with MAGPHYS, in Figure 17, and present their physical parameters in Table 4.

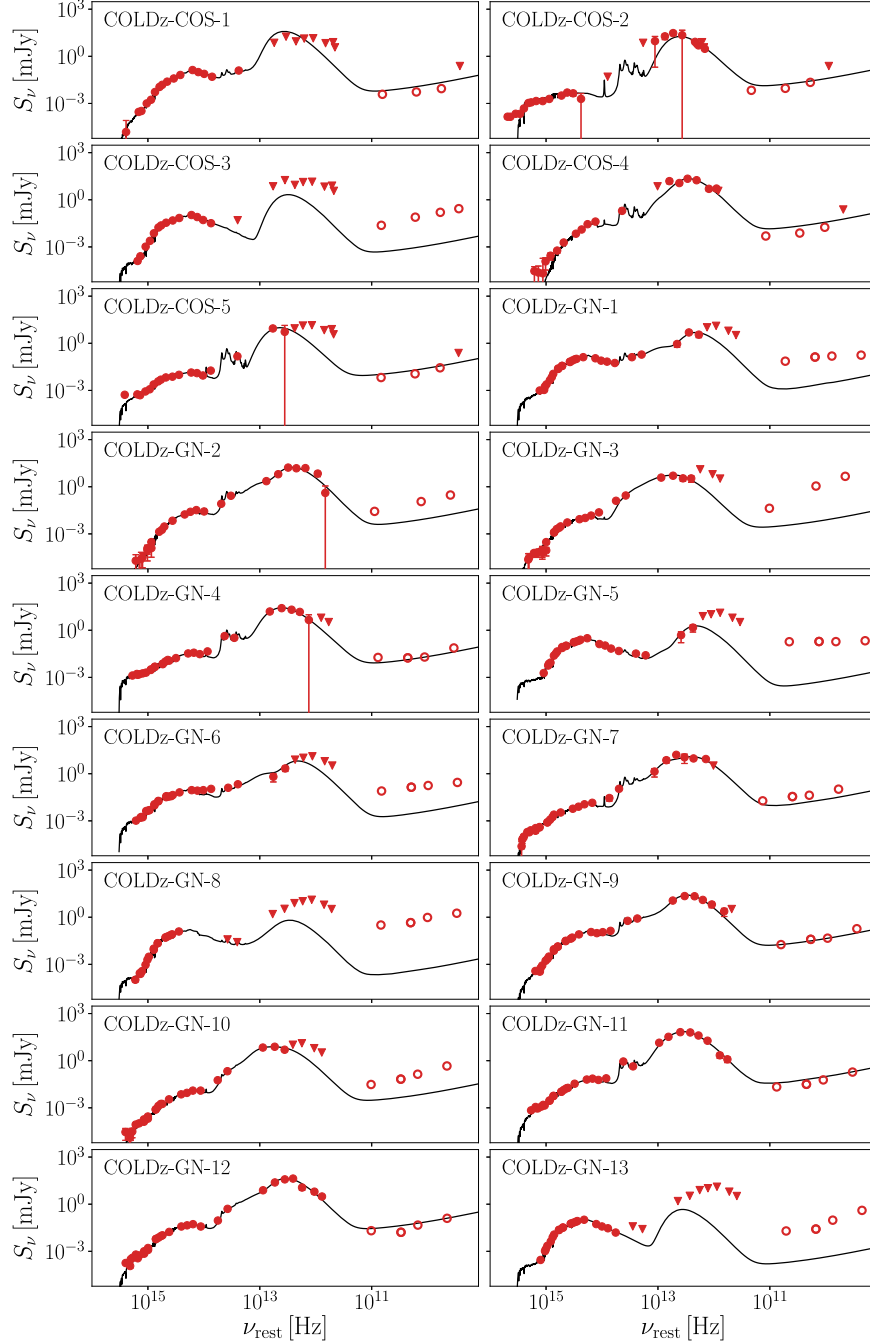


**Figure 17.** The spectral energy distributions of the 18 COLDz continuum detections. All data points are shown in red, with triangles indicating upper limits and open symbols indicating the radio observations, which are not fitted. In half of the sources, the measured radio flux densities lie well above the extrapolated value from MAGPHYS, indicative of additional emission from a radio AGN.

**Table 4**  
Physical Properties of the 34 GHz Selected COLDz Sample

ID	$L_{\text{IR}}$ ( $\log L_{\odot}$ )	SFR <sup>a</sup> ( $\log M_{\odot} \text{ yr}^{-1}$ )	$M_{*}$ ( $\log M_{\odot}$ )	$L_{1.4}^b$ ( $\log \text{W Hz}^{-1}$ )	$q_{\text{IR}}$	AGN <sup>c</sup>
COLDz-cont-COS-1	11.75 <sup>+0.09</sup> <sub>-0.09</sub>	1.40 <sup>+0.14</sup> <sub>-0.06</sub>	11.39 <sup>+0.09</sup> <sub>-0.06</sub>	22.51 <sup>+0.08</sup> <sub>-0.08</sub>	3.25 <sup>+0.12</sup> <sub>-0.12</sub>	0
COLDz-cont-COS-2	13.00 <sup>+0.01</sup> <sub>-0.03</sub>	2.80 <sup>+0.01</sup> <sub>-0.03</sub>	10.78 <sup>+0.02</sup> <sub>-0.03</sub>	24.83 <sup>+0.06</sup> <sub>-0.06</sub>	2.17 <sup>+0.06</sup> <sub>-0.06</sub>	0
COLDz-cont-COS-3	10.70 <sup>+0.19</sup> <sub>-0.51</sub>	0.01 <sup>+0.17</sup> <sub>-0.34</sub>	11.16 <sup>+0.09</sup> <sub>-0.01</sub>	24.04 <sup>+0.04</sup> <sub>-0.04</sub>	0.67 <sup>+0.20</sup> <sub>-0.49</sub>	1
COLDz-cont-COS-4	12.54 <sup>+0.10</sup> <sub>-0.03</sub>	2.21 <sup>+0.21</sup> <sub>-0.40</sub>	11.93 <sup>+0.03</sup> <sub>-0.19</sub>	24.01 <sup>+0.06</sup> <sub>-0.06</sub>	2.56 <sup>+0.10</sup> <sub>-0.08</sub>	0
COLDz-cont-COS-5	11.38 <sup>+0.17</sup> <sub>-0.16</sub>	1.28 <sup>+0.19</sup> <sub>-0.14</sub>	10.23 <sup>+0.05</sup> <sub>-0.08</sub>	23.32 <sup>+0.03</sup> <sub>-0.03</sub>	2.08 <sup>+0.17</sup> <sub>-0.17</sub>	0
COLDz-cont-GN-1	10.66 <sup>+0.07</sup> <sub>-0.03</sub>	0.31 <sup>+0.08</sup> <sub>-0.11</sub>	11.04 <sup>+0.05</sup> <sub>-0.03</sub>	23.17 <sup>+0.02</sup> <sub>-0.02</sub>	1.51 <sup>+0.06</sup> <sub>-0.04</sub>	1
COLDz-cont-GN-2	12.12 <sup>+0.02</sup> <sub>-0.02</sub>	1.84 <sup>+0.07</sup> <sub>-0.12</sub>	11.47 <sup>+0.11</sup> <sub>-0.09</sub>	24.63 <sup>+0.13</sup> <sub>-0.05</sub>	1.49 <sup>+0.05</sup> <sub>-0.13</sub>	1
COLDz-cont-GN-3	12.27 <sup>+0.01</sup> <sub>-0.01</sub>	1.92 <sup>+0.01</sup> <sub>-0.01</sub>	11.01 <sup>+0.01</sup> <sub>-0.01</sub>	26.18 <sup>+0.02</sup> <sub>-0.02</sub>	0.10 <sup>+0.02</sup> <sub>-0.02</sub>	1
COLDz-cont-GN-4	12.23 <sup>+0.01</sup> <sub>-0.01</sub>	1.73 <sup>+0.01</sup> <sub>-0.01</sub>	10.64 <sup>+0.01</sup> <sub>-0.01</sub>	23.86 <sup>+0.09</sup> <sub>-0.09</sub>	2.37 <sup>+0.09</sup> <sub>-0.09</sub>	0
COLDz-cont-GN-5	9.34 <sup>+0.21</sup> <sub>-0.01</sub>	-0.88 <sup>+0.17</sup> <sub>-0.10</sub>	10.83 <sup>+0.09</sup> <sub>-0.06</sub>	22.75 <sup>+0.02</sup> <sub>-0.02</sub>	0.62 <sup>+0.18</sup> <sub>-0.04</sub>	1
COLDz-cont-GN-6	11.23 <sup>+0.04</sup> <sub>-0.10</sub>	1.11 <sup>+0.01</sup> <sub>-0.11</sub>	11.06 <sup>+0.05</sup> <sub>-0.02</sub>	23.93 <sup>+0.02</sup> <sub>-0.02</sub>	1.30 <sup>+0.05</sup> <sub>-0.10</sub>	1
COLDz-cont-GN-7	12.60 <sup>+0.04</sup> <sub>-0.07</sub>	2.54 <sup>+0.07</sup> <sub>-0.05</sub>	10.81 <sup>+0.03</sup> <sub>-0.07</sub>	24.72 <sup>+0.10</sup> <sub>-0.09</sub>	1.88 <sup>+0.11</sup> <sub>-0.12</sub>	0
COLDz-cont-GN-8	10.38 <sup>+1.31</sup> <sub>-0.04</sub>	-0.15 <sup>+1.01</sup> <sub>-0.13</sub>	11.56 <sup>+0.01</sup> <sub>-0.12</sub>	24.83 <sup>+0.03</sup> <sub>-0.03</sub>	-0.40 <sup>+1.25</sup> <sub>-0.09</sub>	1
COLDz-cont-GN-9	11.82 <sup>+0.03</sup> <sub>-0.01</sub>	1.56 <sup>+0.02</sup> <sub>-0.01</sub>	11.23 <sup>+0.14</sup> <sub>-0.01</sub>	23.85 <sup>+0.03</sup> <sub>-0.03</sub>	1.99 <sup>+0.04</sup> <sub>-0.03</sub>	0
COLDz-cont-GN-10	12.37 <sup>+0.01</sup> <sub>-0.01</sub>	2.34 <sup>+0.01</sup> <sub>-0.01</sub>	10.59 <sup>+0.06</sup> <sub>-0.01</sub>	25.11 <sup>+0.02</sup> <sub>-0.02</sub>	1.26 <sup>+0.02</sup> <sub>-0.02</sub>	1
COLDz-cont-GN-11	12.58 <sup>+0.01</sup> <sub>-0.01</sub>	2.59 <sup>+0.01</sup> <sub>-0.01</sub>	11.01 <sup>+0.01</sup> <sub>-0.01</sub>	24.17 <sup>+0.03</sup> <sub>-0.03</sub>	2.42 <sup>+0.03</sup> <sub>-0.03</sub>	0
COLDz-cont-GN-12	12.78 <sup>+0.01</sup> <sub>-0.02</sub>	2.65 <sup>+0.02</sup> <sub>-0.01</sub>	11.59 <sup>+0.01</sup> <sub>-0.12</sub>	24.46 <sup>+0.08</sup> <sub>-0.07</sub>	2.32 <sup>+0.07</sup> <sub>-0.08</sub>	0
COLDz-cont-GN-13	9.43 <sup>+0.10</sup> <sub>-0.15</sub>	-1.00 <sup>+0.11</sup> <sub>-0.08</sub>	10.77 <sup>+0.02</sup> <sub>-0.03</sub>	23.62 <sup>+0.03</sup> <sub>-0.03</sub>	-0.19 <sup>+0.10</sup> <sub>-0.15</sub>	1












#### Notes.

<sup>a</sup> The star formation rate as determined via MAGPHYS.

<sup>b</sup> The radio luminosity at rest-frame 1.4 GHz is computed using the closest observed-frame flux density (1.4 or 3 GHz) and the measured radio spectral index.

<sup>c</sup> Sources are identified as radio AGNs based on their offset from the FIRRC (Section 6.1).

#### ORCID iDs

H. S. B. Algera  <https://orcid.org/0000-0002-4205-9567>  
J. A. Hodge  <https://orcid.org/0000-0001-6586-8845>  
D. Riechers  <https://orcid.org/0000-0001-9585-1462>  
E. J. Murphy  <https://orcid.org/0000-0001-7089-7325>  
R. Pavesi  <https://orcid.org/0000-0002-2263-646X>  
M. Aravena  <https://orcid.org/0000-0002-6290-3198>  
E. Daddi  <https://orcid.org/0000-0002-3331-9590>  
R. Decarli  <https://orcid.org/0000-0002-2662-8803>  
M. Dickinson  <https://orcid.org/0000-0001-5414-5131>  
M. Sargent  <https://orcid.org/0000-0003-1033-9684>  
C. E. Sharon  <https://orcid.org/0000-0002-6250-5608>

#### References

- Alexander, D. M., Bauer, F. E., Chapman, S. C., et al. 2005, *ApJ*, **632**, 736  
Algera, H. S. B., Smail, I., Dudzevičiūtė, U., et al. 2020a, *ApJ*, **903**, 138  
Algera, H. S. B., van der Vlugt, D., Hodge, J. A., et al. 2020b, *ApJ*, **903**, 139  
Aravena, M., Murphy, E. J., Aguirre, J. E., et al. 2013, *MNRAS*, **433**, 498  
Ashby, M. L. N., Willner, S. P., Fazio, G. G., et al. 2013, *ApJ*, **769**, 80  
Barger, A. J., Kohno, K., Murphy, E. J., Sargent, M. T., & Condon, J. J. 2018, arXiv:1810.07143  
Battisti, A. J., da Cunha, E., Grasha, K., et al. 2019, *ApJ*, **882**, 61  
Bell, E. F. 2003, *ApJ*, **586**, 794  
Bonaldi, A., Bonato, M., Galluzzi, V., et al. 2019, *MNRAS*, **482**, 2  
Bondi, M., Ciliegi, P., Schinnerer, E., et al. 2008, *ApJ*, **681**, 1129  
Bonzini, M., Padovani, P., Mainieri, V., et al. 2013, *MNRAS*, **436**, 3759  
Brammer, G. B., van Dokkum, P. G., Franx, M., et al. 2012, *ApJS*, **200**, 13  
Braun, R., Bonaldi, A., Bourke, T., Keane, E., & Wagg, J. 2019, arXiv:1912.12699  
Bressan, A., Silva, L., & Granato, G. L. 2002, *A&A*, **392**, 377  
Butler, B., Grammer, W., Selina, R., Carilli, C., & Murphy, E. J. 2019, AAS Meeting, **233**, 361.10  
Calistro Rivera, G., Williams, W. L., Hardcastle, M. J., et al. 2017, *MNRAS*, **469**, 3468  
Carilli, C. L., Perley, R. A., Dreher, J. W., & Leahy, J. P. 1991, *ApJ*, **383**, 554  
Chabrier, G. 2003, *PASP*, **115**, 763  
Civano, F., Marchesi, S., Comastri, A., et al. 2016, *ApJ*, **819**, 62  
Condon, J. J. 1992, *ARA&A*, **30**, 575  
Condon, J. J. 1997, *PASP*, **109**, 166  
Condon, J. J., Cotton, W. D., Greisen, E. W., et al. 1998, *AJ*, **115**, 1693  
Condon, J. J., & Mitchell, K. J. 1984, *AJ*, **89**, 610  
Cotton, W. D., Condon, J. J., Kellermann, K. I., et al. 2018, *ApJ*, **856**, 67  
da Cunha, E., Charlot, S., & Elbaz, D. 2008, *MNRAS*, **388**, 1595  
da Cunha, E., Walter, F., Smail, I. R., et al. 2015, *ApJ*, **806**, 110  
Daddi, E., Dannerbauer, H., Krips, M., et al. 2009, *ApJL*, **695**, L176  
Decarli, R., Walter, F., Aravena, M., et al. 2016, *ApJ*, **833**, 70  
Decarli, R., Walter, F., Carilli, C., et al. 2014, *ApJ*, **782**, 78  
de Jong, T., Klein, U., Wielebinski, R., & Wunderlich, E. 1985, *A&A*, **147**, L6  
Delhaize, J., Smolčić, V., Delvecchio, I., et al. 2017, *A&A*, **602**, A4  
Delvecchio, I., Daddi, E., Sargent, M. T., et al. 2021, *A&A*, **647**, A123  
Delvecchio, I., Smolčić, V., Zamorani, G., et al. 2017, *A&A*, **602**, A3  
Dickinson, M., Giavalisco, M., & GOODS Team 2003, in *The Mass of Galaxies at Low and High Redshift*, ed. R. Bender & A. Renzini (Berlin: Springer), 324  
Donley, J. L., Koekemoer, A. M., Brusa, M., et al. 2012, *ApJ*, **748**, 142  
Dopita, M. A., Groves, B. A., Sutherland, R. S., & Kewley, L. J. 2003, *ApJ*, **583**, 727  
Elbaz, D., Dickinson, M., Hwang, H. S., et al. 2011, *A&A*, **533**, A119  
Frayser, D. T., Koda, J., Pope, A., et al. 2008, *ApJL*, **680**, L21  
Geach, J. E., Dunlop, J. S., Halpern, M., et al. 2017, *MNRAS*, **465**, 1789  
Gehrels, N. 1986, *ApJ*, **303**, 336  
Giavalisco, M., Ferguson, H. C., Koekemoer, A. M., et al. 2004, *ApJL*, **600**, L93  
Gim, H. B., Yun, M. S., Owen, F. N., et al. 2019, *ApJ*, **875**, 80  
Helou, G., Soifer, B. T., & Rowan-Robinson, M. 1985, *ApJL*, **298**, L7  
Huyh, M. T., Emonts, B. H. C., Kimball, A. E., et al. 2017, *MNRAS*, **467**, 1222  
Inoue, A. K., Hirashita, H., & Kamaya, H. 2001, *ApJ*, **555**, 613  
Jiménez-Andrade, E. F., Magnelli, B., Karim, A., et al. 2019, *A&A*, **625**, A114  
Jin, S., Daddi, E., Liu, D., et al. 2018, *ApJ*, **864**, 56  
Kennicutt, R. C., Jr+ 1998, *ARA&A*, **36**, 189  
Klein, U., Lisenfeld, U., & Verley, S. 2018, *A&A*, **611**, A55  
Laigle, C., McCracken, H. J., Ilbert, O., et al. 2016, *ApJS*, **224**, 24  
Linden, S. T., Murphy, E. J., Dong, D., et al. 2020, *ApJS*, **248**, 25  
Liu, D., Daddi, E., Dickinson, M., et al. 2018, *ApJ*, **853**, 172

- Liu, D., Schinnerer, E., Groves, B., et al. 2019, *ApJ*, **887**, 235
- Magnelli, B., Popesso, P., Berta, S., et al. 2013, *A&A*, **553**, A132
- Mahatma, V. H., Hardcastle, M. J., Williams, W. L., et al. 2018, *MNRAS*, **475**, 4557
- Marchesi, S., Civano, F., Elvis, M., et al. 2016, *ApJ*, **817**, 34
- Mason, B. S., Weintraub, L., Sievers, J., et al. 2009, *ApJ*, **704**, 1433
- McKinnon, M., Beasley, A., Murphy, E., et al. 2019, *BAAS*, **51**, 81
- Mohan, N., & Rafferty, D. 2015, PyBDSF: Python Blob Detection and Source Finder, Astrophysics Source Code Library, ascl:1502.007
- Molnár, D. C., Sargent, M. T., Delhaize, J., et al. 2018, *MNRAS*, **475**, 827
- Momcheva, I. G., Brammer, G. B., van Dokkum, P. G., et al. 2016, *ApJS*, **225**, 27
- Morrison, G. E., Owen, F. N., Dickinson, M., Ivison, R. J., & Ibar, E. 2010, *ApJS*, **188**, 178
- Murphy, E. J., Bolatto, A., Chatterjee, S., et al. 2018, in ASP Conf. Ser. 517, Science with a Next Generation Very Large, ed. E. Murphy (San Francisco, CA: ASP), 3, arXiv:1810.07524
- Murphy, E. J., Bremseth, J., Mason, B. S., et al. 2012, *ApJ*, **761**, 97
- Murphy, E. J., & Chary, R.-R. 2018, *ApJ*, **861**, 27
- Murphy, E. J., Condon, J. J., Schinnerer, E., et al. 2011, *ApJ*, **737**, 67
- Murphy, E. J., Momjian, E., Condon, J. J., et al. 2017, *ApJ*, **839**, 35
- Niklas, S., Klein, U., & Wielebinski, R. 1997, *A&A*, **322**, 19
- Ocran, E. F., Taylor, A. R., Vaccari, M., et al. 2020, *MNRAS*, **491**, 5911
- Owen, F. N. 2018, *ApJS*, **235**, 34
- Padovani, P., Mainieri, V., Tozzi, P., et al. 2009, *ApJ*, **694**, 235
- Pavesi, R., Riechers, D. A., Capak, P. L., et al. 2016, *ApJ*, **832**, 151
- Pavesi, R., Sharon, C. E., Riechers, D. A., et al. 2018, *ApJ*, **864**, 49
- Penner, K., Pope, A., Chapin, E. L., et al. 2011, *MNRAS*, **410**, 2749
- Penney, J. I., Blain, A. W., Assef, R. J., et al. 2020, *MNRAS*, **496**, 1565
- Pope, A., Borys, C., Scott, D., et al. 2005, *MNRAS*, **358**, 149
- Querejeta, M., Schinnerer, E., Schrubba, A., et al. 2019, *A&A*, **625**, A19
- Read, S. C., Smith, D. J. B., Gürkan, G., et al. 2018, *MNRAS*, **480**, 5625
- Riechers, D. A., Bradford, C. M., Clements, D. L., et al. 2013, *Natur*, **496**, 329
- Riechers, D. A., Hodge, J. A., Pavesi, R., et al. 2020, *ApJ*, **895**, 81
- Riechers, D. A., Pavesi, R., Sharon, C. E., et al. 2019, *ApJ*, **872**, 7
- Rowan-Robinson, M., Benn, C. R., Lawrence, A., McMahon, R. G., & Broadhurst, T. J. 1993, *MNRAS*, **263**, 123
- Schinnerer, E., Sargent, M. T., Bondi, M., et al. 2010, *ApJS*, **188**, 384
- Schinnerer, E., Smolčić, V., Carilli, C. L., et al. 2007, *ApJS*, **172**, 46
- Scoville, N., Aussel, H., Brusa, M., et al. 2007, *ApJS*, **172**, 1
- Seymour, N., McHardy, I. M., & Gunn, K. F. 2004, *MNRAS*, **352**, 131
- Simpson, J. M., Smail, I., Dudzevičiūtė, U., et al. 2020, *MNRAS*, **495**, 3409
- Skelton, R. E., Whitaker, K. E., Momcheva, I. G., et al. 2014, *ApJS*, **214**, 24
- Smolčić, V., Delvecchio, I., Zamorani, G., et al. 2017, *A&A*, **602**, A2
- Smolčić, V., Novak, M., Bondi, M., et al. 2017, *A&A*, **602**, A1
- Stach, S. M., Dudzevičiūtė, U., Smail, I., et al. 2019, *MNRAS*, **487**, 4648
- Symeonidis, M., Georgakakis, A., Page, M. J., et al. 2014, *MNRAS*, **443**, 3728
- Tabatabaei, F. S., Schinnerer, E., Krause, M., et al. 2017, *ApJ*, **836**, 185
- Tabatabaei, F. S., Schinnerer, E., Murphy, E. J., et al. 2013, *A&A*, **552**, A19
- Thomson, A. P., Ivison, R. J., Smail, I., et al. 2012, *MNRAS*, **425**, 2203
- Thomson, A. P., Smail, I., Swinbank, A. M., et al. 2019, *ApJ*, **883**, 204
- Tisanić, K., Smolčić, V., Delhaize, J., et al. 2019, *A&A*, **621**, A139
- van der Kruit, P. C. 1971, *A&A*, **15**, 110
- van der Kruit, P. C. 1973, *A&A*, **29**, 263
- van der Vlugt, D., Algera, H. S. B., Hodge, J. A., et al. 2021, *ApJ*, **907**, 5
- Wagg, J., Carilli, C. L., Aravena, M., et al. 2014, *ApJ*, **783**, 71
- Walter, F., Decarli, R., Aravena, M., et al. 2016, *ApJ*, **833**, 67
- Wilman, R. J., Miller, L., Jarvis, M. J., et al. 2008, *MNRAS*, **388**, 1335
- Xue, Y. Q., Luo, B., Brandt, W. N., et al. 2016, *ApJS*, **224**, 15
- Yun, M. S., Reddy, N. A., & Condon, J. J. 2001, *ApJ*, **554**, 803